Journal of Computational Physics **154,** 428–467 (1999)
Article ID jcph.1999.6322, available online at http://www.idealibrary.com on IDEAL®

A Semi-implicit Numerical Scheme for Reacting Flow[1]

II. Stiff, Operator-Split Formulation

Omar M. Knio,* Habib N. Najm,† and Peter S. Wyckoff†

**Department of Mechanical Engineering, The Johns Hopkins University, Baltimore, Maryland 21218-2686; and †Combustion Research Facility, Sandia National Laboratories, Livermore, California 94551*
E-mail: knio@jhu.edu and hnnajm@ca.sandia.gov

Received February 10, 1999; revised June 21, 1999

A stiff,[1] operator-split projection scheme is constructed for the simulation of unsteady two-dimensional reacting flow with detailed kinetics. The scheme is based on the compressible conservation equations for an ideal gas mixture in the zero-Mach-number limit. The equations of motion are spatially discretized using second-order centered differences and are advanced in time using a new stiff predictor–corrector approach. The new scheme is a modified version of the additive, stiff scheme introduced in a previous effort by H. N. Najm, P. S. Wyckoff, and O. M. Knio (1998, *J. Comput. Phys.* **143**, 381). The predictor updates the scalar fields using a Strang-type operator-split integration step which combines several explicit diffusion sub-steps with a single stiff step for the reaction terms, such that the global time step may significantly exceed the critical diffusion stability limit. Convection terms are explicitly handled using a second-order multi-step scheme. The velocity field is advanced using a projection scheme which consists of a partial convection–diffusion update followed by a pressure correction step. A split approach is also adopted for the convection–diffusion step in the momentum update. This splitting combines an explicit treatment of the convective terms at the global time step with several explicit fractional steps for diffusion. Finally, a corrector step is implemented in order to couple the evolution of the density and velocity fields and to stabilize the computations. The corrector acts only on the convective terms and the pressure field, while the predicted updates due to diffusion and reaction are left unchanged. The correction of the scalar fields is implemented using a single-step non-split, non-stiff, second-order time integration. A similar procedure is used for the velocity field, which is followed

[1] The U.S. Government's right to retain a nonexclusive royalty-free license in and to the copyright covering this paper, for governmental purposes, is acknowledged.

0021-9991/99 $30.00

by a pressure projection step. The performance and behavior of the operator-split scheme are first analyzed based on tests for a nonlinear reaction–diffusion equation in one space dimension, followed by computations with a detailed C_1C_2 methane–air mechanism in one and two dimensions. The tests are used to verify that the scheme is effectively second order in time, and to suggest guidelines for selecting integration parameters, including the number of fractional diffusion steps and tolerance levels in the stiff integration. For two-dimensional simulations with the present reaction mechanism, flame conditions, and resolution parameters, speedup factors of about 5 are achieved over the previous additive scheme, and about 25 over the original explicit scheme.

Key Words: implicit; stiff; operator splitting; chemistry; reacting; flow; projection.

1. INTRODUCTION

The modeling of chemically reacting flow presents pronounced difficulties associated with the inherently large ranges of spatial and temporal scales involved, the corresponding resolution requirements, and the stiffness of the governing differential equations. Stiff governing equations [1, 2] arise in diverse applications, including chemically reacting flow, energetic materials, electrical circuits, atmospheric modeling, and biological systems. In general, these stiff systems present significant challenges to computational simulations, typically manifested in very small time step size restrictions.

The manifestation and symptoms of stiffness obviously depend on the nature of the application. In this work, we focus on the numerical simulation of unsteady two-dimensional (2D) flow of a premixed reacting hydrocarbon mixture with detailed chemical kinetics. The manifestation of stiffness in this application is discussed below in light of an illustrative example of a methane–air flame at atmospheric pressure. In addition to the wide disparity between various chemical time scales, the flame has a fine spatial structure, requiring a computational cell size of 16 μm or less for adequate resolution. For this spatial resolution level, the critical H-atom diffusion stability limit for an explicit second-order Runge–Kutta (RK2) scheme in 2D is around 20 ns. Depending on the particular chemical mechanism, the time step limitation due to reaction rate stiffness may be below or above this value. We have found that explicit time integration of C_1C_2 kinetics (GRImech1.2 [3]) necessitates a time step smaller than 2 ns [4] for this flame, while the integration of a "skeletal" C_1 mechanism [5] is possible with the 20 ns diffusion-limited time step. Thus as the complexity of the reaction mechanism increases, the temporal stiffness associated with chemical source terms can become significantly more pronounced.

Stiffness limitations are typically overcome by adopting a stiff-integration scheme or a specially tailored integration method. A variety of approaches have been used to construct different classes of stiff solvers. A well-known approach is to rely on backward-difference formulas (BDFs) [6]; these have been used as a basis for several stiff ODE integration packages, including GEAR [7, 8], GEARB [9], LSODE [10, 11], and VODE [12]. Although widespread, the use of BDFs is by no means the only possible, or necessarily most suitable, approach. A variety of alternatives have also been proposed. Examples include implicit or semi-implicit Runge–Kutta schemes (e.g., [13–15]), higher-order Taylor methods (e.g., [16]), as well as specialized methods that are based on segregation of "fast" and "slow" variables (e.g., [17–24]).

The selection of a suitable stiff time-integration approach should be carefully performed, and must account for the nature of the problem and the properties of the associated model. For the currently targeted detailed kinetics computations a key factor is the complexity of the chemical mechanism, which may involve large numbers of species and elementary reaction steps. Consequently, evaluation of chemical source terms is computationally expensive; this is relevant for the choice of stiff time-integration scheme which must enable accurate computations with large, stable time steps *without* requiring an excessive number of functional iterations. This feature has, in many situations involving stiff chemical reactions, favored the selection of a BDF-based integration approach [25–27, 23, 28], and, when possible, motivated the incorporation of specialized nonlinear equation solvers (e.g., [29–31]). For a more detailed discussion, see [25, 4].

It should be emphasized, however, that incorporation of a stiff solver into a reacting flow code is not straightforward, in large part because of the coupling between the reaction term and the diffusion and convective transport terms. The presence of convective terms is generally not problematic, since the selection of convective CFL numbers [32, 33] well below unity is desirable anyway, in order to maintain small phase errors [34]. Thus, an explicit treatment of convective terms is in most cases suitable. The treatment of the diffusion term, on the other hand, is a more delicate issue. On the one hand, an implicit treatment of diffusion would be desirable in order to overcome the stability restriction of an explicit solver. However, unless the diffusion coefficients are assumed constant, their dependence on the temperature (and possibly species concentrations) couples the diffusion terms in all the scalar evolution equations. In two and three dimensions, this leads to a very large system of coupled nonlinear equations, whose solution would require large memory capacities, involve large communication costs on parallel machines, and may necessitate the implementation of specialized nonlinear equation solvers.

The above considerations suggest that "hybrid" implicit–explicit (IMEX) approaches, in which individual terms in the governing equations are integrated using specialized schemes, may be particularly advantageous. These non-split schemes have been used extensively in the literature, e.g., [35–42]. Different versions have been studied and compared against each other [43, 38, 40, 36, 41, 42, 44]. Our previous work [4] featured the construction and implementation of a semi-implicit, additive, stiff scheme for the simulation of 2D reacting flow with detailed kinetics. The numerical formulation in [4] uses a predictor–corrector methodology; the predictor uses an explicit linear multi-step method while the corrector incorporates a stiff ODE method for the treatment of chemical source terms. The scheme was applied to the simulation of premixed methane–air flames [45]. The computations have shown that the scheme efficiently overcomes the chemical stiffness of the equations of motion and results in significant speedup over its explicit predecessor. However, since the diffusion terms are handled explicitly in [4], the time step could not be increased beyond the diffusion stability limit. The objective of the present effort is to explore a new construction which overcomes this limitation and leads to further CPU-time savings.

To this end, we have initially considered the implementation of a fully implicit diffusion solver, a directional splitting technique, and an operator-splitting method. Due in large part to the computational difficulties discussed above, the last approach was adopted. Starting from the previous construction in [4], we seek to overcome the diffusive stiffness of the equations by integrating the diffusion terms in several fractional steps, such that the global time step can be significantly larger than the diffusion stability limit. This approach appears

to be well suited to simulations of stiff detailed kinetics, since the CPU time is dominated by the evaluation of reaction source terms.

The utility of operator-splitting techniques derives from the advantage of the sequential application of individual operators. Thus, the integration procedure over each split time step can be optimized for individual operators independently, and computational efficiency can be consequently enhanced. Operator-splitting techniques have been widely utilized in atmospheric modeling studies [46–48, 37, 49, 40, 50, 51] to decouple reaction from diffusion and convection terms, diffusion plus reaction from convection, and to decouple operators in different spatial dimensions. Emphasis has been placed on the stability of different operator-splitting schemes [46, 52, 53] and the role of stiffness in stability [54]. The identification and control of splitting errors has been a common subject of investigation [46, 47, 37, 49, 55, 51]. To date, the symmetric Strang [56] splitting approach for achieving second-order accuracy has been most commonly and successfully used. Higher-order splitting approaches have been reported [57, 46, 58, 52], but have generally been found to exhibit considerable stability-related problems due to negative time stepping (the stability of operator-split schemes has been discussed in [46, 52, 53]). Operator-split schemes have been compared against IMEX [37, 40] and other operator-splitting approaches [50, 51]. Sub-stepping (sub-cycling) has been used both in the split stiff reaction term integration and in the integration of the diffusion or convection terms [47, 37, 51]. Note that the application of stiff integrators in the context of an operator-split construction requires particular attention to the resulting transients [50] in the stiff integration procedure and the consequences of restarting the stiff ODE integrator [48, 40] at each time step.

There is some computational evidence concerning the behavior and performance of operator-split schemes for flames [59, 60], and some focus on the role of stiff integrators therein [28]. For instance, the splitting can result in a globally first-order scheme [59, 28], which raises questions regarding the accuracy of the computations. In [60], a Strang-type symmetric splitting is used to construct a formally second-order scheme, but the computational tests show that only superlinear convergence is achieved. Thus, it is also essential that the behavior of stiff operator-split approaches in flames be thoroughly tested and their performance carefully established.

As mentioned earlier, this paper explores the use of operator splitting to enhance the efficiency of simulation of premixed hydrocarbon flames with detailed kinetics. It is organized as follows: In Section 2, we provide a brief overview of the governing equations for zero-Mach-number combustion. In Section 3, we describe an operator-split extension of our previous stiff scheme from [4]. The essential aspect of the present extension is the replacement of the explicit predictor with a symmetrically split, stiff solver. In Section 4, the performance of the new predictor is examined based on detailed tests of a one-dimensional, nonlinear reaction–diffusion equation. The tests are used to clearly establish the convergence properties of the scheme and to analyze the effect of splitting parameters and the tolerances used in the stiff integrator. The full scheme is applied in Section 5 to the simulation of premixed methane–air flames in one and two space dimensions. The simulation uses the C_1C_2 mechanism GRImech1.2 [3], which involves 32 species and 177 elementary reactions. These tests are used to further examine the results established in Section 4 and to investigate the speedup gained in the computations. A discussion of the present experiences is provided in Section 6, together with a summary of major conclusions.

2. FORMULATION

As in [4], a simplified physical model is used that is based on the zero-Mach-number limit of the compressible conservation equations [61]. In this limit, acoustic waves are ignored and the pressure field is decomposed into a spatially uniform component $P_0(t)$ and a hydrodynamic component $p(\mathbf{x}, t)$ which varies both in space and in time. We assume a 2D open domain, a gas mixture with zero bulk viscosity [62], and a detailed chemical kinetic mechanism involving N species and K elementary reactions. Soret and Dufour effects [63] are ignored, as well as body forces and radiant heat transfer.

Under the above assumptions, the evolution of the flow field is governed by the mass, momentum, energy, and species conservation equations, which are expressed in non-dimensional form as

$$\frac{\partial \rho}{\partial t} + \nabla \cdot (\rho \mathbf{v}) = 0 \tag{1}$$

$$\frac{\partial (\rho u)}{\partial t} + \frac{\partial (\rho u^2)}{\partial x} + \frac{\partial (\rho u v)}{\partial y} = -\frac{\partial p}{\partial x} + \frac{1}{\mathrm{Re}} \Phi_x \tag{2}$$

$$\frac{\partial (\rho v)}{\partial t} + \frac{\partial (\rho v u)}{\partial x} + \frac{\partial (\rho v^2)}{\partial y} = -\frac{\partial p}{\partial y} + \frac{1}{\mathrm{Re}} \Phi_y \tag{3}$$

$$\frac{\partial T}{\partial t} + \mathbf{v} \cdot \nabla T = \frac{1}{\mathrm{Re\,Pr}} \frac{\nabla \cdot (\lambda \nabla T)}{\rho c_p} + \frac{1}{\mathrm{Re\,Sc}} \frac{\mathbf{Z} \cdot \nabla T}{c_p} + \mathrm{Da}\, \frac{w_T}{\rho c_p} \tag{4}$$

$$\frac{\partial (\rho Y_i)}{\partial T} = -\nabla \cdot (\rho \mathbf{v} Y_i) + \frac{1}{\mathrm{Re\,Sc}} \nabla \cdot (\rho D_{iN} \nabla Y_i) + \mathrm{Da}\, w_i, \tag{5}$$

respectively. Here, ρ is the density, T is the temperature, $\mathbf{v} = (u, v)$ is the velocity vector, Y_i is the mass fraction of species i, μ is the dynamic viscosity, λ is the thermal conductivity, c_p is the mixture specific heat, w_i is the chemical production rate of species i, w_T is rate of chemical heat release, Re, Pr, Sc, and Da are the Reynolds, Prandtl, Schmidt, and Damköhler numbers, respectively, while Φ_x,Φ_y are the viscous stress terms.

The mixture is assumed to obey the perfect gas law, with individual species molecular weights, specific heats, and enthalpies of formation. The equation of state is expressed as

$$P_0 = \rho T / \bar{W}, \tag{6}$$

where $\bar{W} \equiv 1/(\sum_{i=1}^{N} Y_i / W_i)$ is the local effective molar mass of the mixture, and W_i is the molecular weight of species i. Note that for an open domain P_0 is constant, while p varies in space and time [4]. The specific heat of the mixture is given by

$$c_p = \sum_{i=1}^{N} Y_i c_{p,i}, \tag{7}$$

where $c_{p,i}$ is the specific heat of the ith species at constant pressure.

The Nth species, here N_2, is assumed dominant such that the diffusion velocity of any other species $i \neq N$ in the mixture is approximated by $\mathbf{V}_i = -D_{iN} \nabla Y_i / Y_i$, where D_{iN} is the binary mass diffusion coefficient of species i into the Nth species at the mixture local temperature and stagnation pressure. $\mathbf{V}_N$ is found from the identity $\sum_{i=1}^{N} Y_i \mathbf{V}_i \equiv 0$ [63]. Similarly, the mass fraction Y_N is obtained from the identity $\sum_{i=1}^{N} Y_i \equiv 1$. Meanwhile, $\mathbf{Z}$

is defined by $\mathbf{Z} \equiv \sum_{i=1}^{N} c_{p,i} D_{iN} \nabla Y_i$. Note that the above approximation of $\mathbf{V}_i$ assumes that $Y_i \ll Y_N$, $i = 1, \ldots, N-1$, i.e., that species $i = 1, \ldots, N-1$ are traces in species N. Finally, for computational efficiency, the mixture transport properties (μ, λ) are set to those of the dominant species at the local temperature.

The production rate for each species (w_i) is given by the sum of contributions of elementary reactions [63], with Arrhenius rates $r_k = A_k T^{b_k} e^{-E_k/RT}$, $k = 1, \ldots, K$. The overall progress of an elementary reaction accounts for both forward and backward rates, corrections for third body efficiencies, and pressure dependence [64]. The heat release term is given by

$$w_T = -\sum_{i=1}^{N} h_i w_i, \tag{8}$$

where $h_i = h_i^o + \int_{T^o}^{T} c_{p,i}\, dT$ is the enthalpy of species i, and the superscript o is used to denote known reference conditions.

Finally, for the purpose of the numerical implementation described below, the time rate of change of density is found by differentiating the equation of state,

$$\frac{\partial \rho}{\partial t} = \rho \left(-\frac{1}{T}\frac{\partial T}{\partial t} - \bar{W} \sum_{i=1}^{N} \frac{1}{W_i} \frac{\partial Y_i}{\partial t} \right), \tag{9}$$

and substituting for $\partial T/\partial t$ and $\partial Y_i/\partial t$ from Eqs. (4) and (5), respectively.

3. NUMERICAL SCHEME

As mentioned in the Introduction, the primary objective of the present effort is to explore an operator-split formulation of the semi-implicit stiff scheme developed in [4]. To this end, we start with a brief summary of the non-split scheme and then outline the present modification.

In both cases, we rely on a projection scheme for variable-density reacting flow. The projection scheme was originally developed by Chorin [65] for the incompressible Navier–Stokes equations. Recently, several variants have been proposed for variable-density (e.g., [66, 67] and reacting flows (e.g., [68–71]). The present formulation is adapted from our previous effort in [4]. We focus on an open 2D domain and rely on a second-order centered finite-difference discretization of the equations of motion. Field variables are discretized using a staggered grid with uniform cell size along each coordinate direction. Velocity components are specified at cell edges, while scalar variables are specified at cell centers.

3.1. Predictor–Corrector Stiff Scheme

The stiff projection scheme from [4] is based on a predictor–corrector integration approach. The predictor uses the explicit, second-order Adams–Bashforth (AB2) scheme to advance the velocity and scalar fields, and incorporates a pressure correction step in order to satisfy conservation of mass. The pressure correction step involves the inversion of a pressure Poisson equation, which is performed using an FFT solver. The corrector, on the other hand, is a mixed, non-split (additive) scheme which combines stiff integration of reaction source terms with second-order Runge–Kutta (RK2) treatment of the remaining

terms. The stiff integrator is adapted from the DVODE package [12] and used in the species equations.

For notational convenience and clarity of the presentation, we first rewrite the species, density, and momentum evolution equations as

$$\frac{\partial(\rho Y_i)}{\partial t} = L_i \equiv C_i + R_i + D_i \tag{10}$$

$$\frac{\partial \rho}{\partial t} = C_\rho + R_\rho + D_\rho + G_\rho \tag{11}$$

$$\frac{\partial(\rho \mathbf{v})}{\partial t} = \mathbf{N}(\rho, \mathbf{v}) + \mathbf{F}(\mu, \mathbf{v}) - \nabla p, \tag{12}$$

where $\mathbf{N}(\rho, \mathbf{v})$ is the momentum convection term, $\mathbf{F}(\mu, \mathbf{v})$ is the viscous force term, while

$$C_i = C_i(\rho, \mathbf{v}, Y_i) \equiv -\nabla \cdot (\rho \mathbf{v} Y_i)$$

$$R_i = R_i(\rho, T, \mathbf{Y}) \equiv \mathrm{Da}\, w_i$$

$$D_i = D_i(\rho, T, Y_i) \equiv \frac{1}{\mathrm{Re}\,\mathrm{Sc}} \nabla \cdot (\rho D_{iN} \nabla Y_i)$$

$$C_\rho \equiv \frac{\rho}{T} \mathbf{v} \cdot \nabla T$$

$$R_\rho \equiv -\frac{1}{c_p T} \mathrm{Da}\, w_T$$

$$D_\rho \equiv -\frac{1}{\mathrm{Re}\,\mathrm{Pr}\, c_p T} \nabla \cdot (\lambda \nabla T) + \frac{\rho}{T} \frac{1}{c_p \mathrm{Re}\,\mathrm{Sc}} \mathbf{Z} \cdot \nabla T$$

$$G_\rho \equiv -\rho C_W$$

$$C_W = \left[\sum_{i=1}^{N} \frac{Y_i}{W_i} \right]^{-1} \sum_{i=1}^{N} \frac{1}{\rho W_i} \left(-\rho \mathbf{v} \cdot \nabla Y_i + \mathrm{Da}\, w_i + \frac{1}{\mathrm{Re}\,\mathrm{Sc}} \nabla \cdot (\rho D_{iN} \nabla Y_i) \right).$$

Using these definitions, the non-split stiff scheme is summarized as follows.

3.1.1. *Explicit Predictor*

N1. Based on the known solution at time level n, the source terms in the species and density evolution equations, namely the fields L_i^n, C_i^n, R_i^n, D_i^n, C_ρ^n, R_ρ^n, D_ρ^n, and G_ρ^n, are evaluated.

N2. Predicted values of the density, $\tilde{\rho}$, species concentrations, $\tilde{Y}_i$, $i = 1, \ldots, N-1$, are determined using the AB2 scheme and predicted values of the temperature are obtained from the equation of state. Thus, we use

$$\frac{\tilde{\rho} - \rho^n}{\Delta t} = \frac{3}{2}\left(C_\rho^n + R_\rho^n + D_\rho^n + G_\rho^n\right) - \frac{1}{2}\left(C_\rho^{n-1} + R_\rho^{n-1} + D_\rho^{n-1} + G_\rho^{n-1}\right) \tag{13}$$

$$\frac{\tilde{\rho}\tilde{Y}_i - \rho^n Y_i^n}{\Delta t} = \frac{3}{2}\left(C_i^n + R_i^n + D_i^n\right) - \frac{1}{2}\left(C_i^{n-1} + R_i^{n-1} + D_i^{n-1}\right) \tag{14}$$

$$\tilde{T} = \frac{P_0 \tilde{\bar{W}}}{\tilde{\rho}}. \tag{15}$$

N3. An intermediate velocity field, $\bar{\mathbf{v}}$, is then determined by integrating the pressure-split

momentum equations [72],

$$\frac{\tilde{\rho}\bar{\mathbf{v}} - \rho^n \mathbf{v}^n}{\Delta t} = \frac{3}{2}(\mathbf{N}^n + \mathbf{F}^n) - \frac{1}{2}(\mathbf{N}^{n-1} + \mathbf{F}^{n-1}). \tag{16}$$

N4. The intermediate hydrodynamic pressure field is determined by inverting the pressure Poisson equation [68],

$$\nabla^2 \tilde{p} = \frac{1}{\Delta t}\left[\nabla \cdot (\tilde{\rho}\bar{\mathbf{v}}) + \left.\frac{\partial \rho}{\partial t}\right|^*\right], \tag{17}$$

where $\partial\rho/\partial t|^*$ is given by the second-order discretization [71]

$$\left.\frac{\partial \rho}{\partial t}\right|^* = \frac{1}{2\Delta t}(3\tilde{\rho} - 4\rho^n + \rho^{n-1}). \tag{18}$$

N5. Finally, the predicted velocity field $\tilde{\mathbf{v}}$ is obtained using the projection step

$$\frac{\tilde{\rho}\tilde{\mathbf{v}} - \tilde{\rho}\bar{\mathbf{v}}}{\Delta t} = -\nabla \tilde{p}. \tag{19}$$

3.1.2. *Stiff, Non-split Corrector*

N6. Corrected values for the scalar fields are obtained using a mixed (non-split) scheme, which combines a stiff treatment of reaction source terms and RK2 treatment of the remaining terms. The problem is formally written, *locally* at each cell center, as a coupled system of N nonlinear evolution equations having the form

$$\frac{\partial(\rho Y_i)}{\partial t} = \frac{1}{2}\left[C_i^n + D_i^n\right] + \frac{1}{2}[C_i(\tilde{\rho}, \tilde{\mathbf{v}}, \tilde{Y}_i) + D_i(\tilde{\rho}, \tilde{T}, \tilde{Y}_i)] + R_i(\rho, T, \mathbf{Y}) \tag{20}$$

$$\frac{\partial \rho}{\partial t} = \frac{1}{2}\left[C_\rho^n + C_\rho(\tilde{\rho}, \tilde{\mathbf{v}}, \tilde{T})\right] + \frac{1}{2}\left[D_\rho^n + D_\rho(\tilde{\rho}, \tilde{T}, \tilde{\mathbf{Y}})\right] - \frac{1}{2}\left[\rho^n \mathcal{C}_W^n + \tilde{\rho}\tilde{\mathcal{C}}_W\right] + \mathcal{R}(\rho, T, \mathbf{Y}), \tag{21}$$

where $\rho\mathbf{Y} = (\rho Y_1, \rho Y_2, \ldots, \rho Y_{N-1})$ is the reduced local vector of mass concentrations,

$$\mathcal{C}_W \equiv \bar{W}\frac{1}{\rho}\sum_{i=1}^{N} \frac{-\nabla \cdot (\rho \mathbf{v} Y_i) - \frac{1}{\mathrm{Re\,Sc}}\nabla \cdot (\rho Y_i \mathbf{V}_i) + Y_i \nabla \cdot (\rho \mathbf{v})}{W_i} \tag{22}$$

and

$$\mathcal{R}(\rho, T, \mathbf{Y}) \equiv -\frac{1}{c_p T}\mathrm{Da}\, w_T - \bar{W}\sum_{i=1}^{N}\frac{\mathrm{Da}\, w_i}{W_i}. \tag{23}$$

The coupled system (20)–(21) is integrated locally from t_n to t_{n+1} using DVODE [12]. The initial conditions correspond to the scalar values at time level t_n, and the integrations are performed independently at the cell centers where the scalar fields are defined.

N7. An intermediate velocity field $\hat{\mathbf{v}}$ is obtained from the pressure-split momentum equations

$$\frac{\rho^{n+1}\hat{\mathbf{v}} - \rho^n \mathbf{v}^n}{\Delta t} = \frac{3}{2}(\mathbf{N}^n + \mathbf{F}^n) - \frac{1}{2}(\mathbf{N}^{n-1} + \mathbf{F}^{n-1}). \tag{24}$$

This velocity distribution is then corrected using the projection step

$$\frac{\rho^{n+1}\mathbf{v}^{n+1} - \rho^{n+1}\hat{\mathbf{v}}}{\Delta t} = -\nabla \hat{p}\,. \tag{25}$$

$\hat{p}$ is the solution of the pressure Poisson equation

$$\nabla^2 \hat{p} = \frac{1}{\Delta t}\left[\nabla \cdot (\rho^{n+1}\hat{\mathbf{v}}) + \frac{\partial \rho}{\partial t}\bigg|^{**}\right], \tag{26}$$

where

$$\frac{\partial \rho}{\partial t}\bigg|^{**} = \frac{1}{2\Delta t}(3\rho^{n+1} - 4\rho^n - \rho^{n-1}). \tag{27}$$

3.1.3. *Remarks*

1. Performance. The performance of the above additive, semi-implicit stiff scheme was analyzed in detail in our previous work [4]. One- and two-dimensional unsteady tests have shown that the stiff construction efficiently accommodates stiff reactions. In particular, the scheme enables large and stable time steps, achieves second-order convergence in time, and leads to substantial speedup of the computations.

2. Density ratio. The predictor–corrector scheme used above is adapted from the conservative formulation of the compressible zero-Mach-number scheme proposed in [73]. It is indicated in [74] that the corrector enhances the coupling between density, velocity, and hydrodynamic pressure fields and, consequently, the stability of the computations. Without the corrector stage, the computations become unstable when the ratio of maximum to minimum density is roughly larger than 2. When the corrector is used, stable computations have been performed with density ratios as large as 10.

3. Stability. The stiff scheme has been applied extensively to simplified model tests and also in large-scale simulations (e.g., [45, 75]). For the methane–air mechanisms considered, the computations have shown that the time step is restricted by the stability limit associated with the explicit treatment of the diffusion term. This limitation is especially stringent for the present premixed flame simulations which are characterized by a very thin flame structure, leading to fine mesh resolution. Since the stiff integration of the kinetic rate terms could be performed with time steps larger than the critical diffusion limit, it appears that the efficiency of the integration approach can be further increased if this limitation can be overcome or avoided. This possibility, together with our earlier observation that the CPU-time cost is dominated by the kinetic rate evaluations, motivates the development of the splitting approach below.

4. Split-scheme stability. We note that the straightforward application of AB2 or RK2 to the explicit time integration of the isolated scalar diffusion equation leads to time-integration stability viscous-CFL restrictions of $\lambda_{v,c} = 1/2^{n+1}$ and $1/2^n$, respectively, where n is the number of space dimensions. However, the above formulation, involving the coupled AB2–RK2 construction, was empirically found to exhibit the RK2 restriction of $1/2^n$ [4]. Evidently, overall stability is governed more by the stability of the corrector step. As we shall see below, the situation is different when AB2 diffusion sub-steps are implemented in the operator-split construction. The critical viscous-CFL number is found to approach that of AB2 as the number of AB2 sub-steps increases.

5. Treatment of convective terms. As noted in the Introduction, adequate representation of the flame structure of an atmospheric methane–air flame with GRImech1.2 requires cell sizes of 16 μm or smaller. At this resolution, there are about 43 grid points within the flame thermal width of the stoichiometric (20% N_2-diluted) flame considered here. Given the present flow, with characteristic velocities of 2 m/s, we find a corresponding maximum cell Reynolds number of 2.3. In fact, we find both the split and non-split schemes to be stable for cell Reynolds numbers as large as 25. Thus, for the present low-speed flow, the use of a centered convection scheme is quite suitable, and incorporation of upwind discretization is not essential.

3.2. Split, Stiff Scheme

The split scheme is based on symmetric Strang splitting of the diffusion and reaction operators, where two half-time-step integrations of the diffusion term are separated by a full-time-step integration of the reaction term. Moreover, each diffusion 1/2-step is integrated using several fractional sub-steps, thereby allowing the use of a large global time step, several times larger than the critical diffusional time step. Thus, if we denote by M the number of fractional diffusion steps in the integration of the scalar fields, where M is even, let $M' \equiv M/2$ be the number of sub-steps in each scalar diffusion 1/2-step, and define $\Delta t' \equiv \Delta t/M$ as the fractional scalar diffusion time step, then the integration of the scalar diffusion and reaction terms (neglecting convection for now) can be symbolically represented as

$$U^{n+1} = \mathcal{D}_{\Delta t'}^{M'} \mathcal{S}_{\Delta t} \mathcal{D}_{\Delta t'}^{M'} U^n, \tag{28}$$

where U^{n+1} and U^n are discrete solutions at times t_{n+1} and t_n, respectively, $\mathcal{S}_{\Delta t}$ represents the stiff integration of the reaction source term over a step size Δt, and $\mathcal{D}_{\Delta t'}$ represents a fractional diffusion step of size $\Delta t'$. This basic formulation is the basis of the detailed split–stiff scheme construction presented below for the full reacting flow problem.

In order to describe the construction of the complete scheme, we introduce some additional definitions. We denote by L the number of fractional diffusion sub-steps in the integration of the momentum equations, where L may be even or odd. We also introduce the fractional viscous momentum sub-step $\Delta t'' \equiv \Delta t/L$. In addition, we decompose the density source term G_ρ (Eq. (11)) into convective, reactive, and diffusive parts using

$$\begin{aligned} G_\rho &= -C_{W,C} - C_{W,R} - C_{W,D} \\ C_{W,C} &\equiv \bar{W} \sum_{i=1}^{N} -\frac{\rho \mathbf{v} \cdot \nabla Y_i}{W_i} \\ C_{W,R} &\equiv \bar{W} \sum_{i=1}^{N} \frac{\mathrm{Da}\, w_i}{W_i} \\ C_{W,D} &\equiv \bar{W} \sum_{i=1}^{N} \frac{1}{W_i} \frac{1}{\mathrm{Re\,Sc}} \nabla \cdot (\rho D_{iN} \nabla Y_i). \end{aligned} \tag{29}$$

Using these definitions, the operator-split scheme is summarized as follows.

3.2.1. *Stiff Predictor*

S1. Explicit convection source terms for the species (C_i^e) and density (C_ρ^e) evolution equations are evaluated. We rely on the explicit AB2 scheme and set

$$C_i^e = \frac{3}{2}C_i^n - \frac{1}{2}C_i^{n-1} \tag{30}$$

$$S_\rho^e = \frac{3}{2}\left(C_\rho^n - C_{W,C}^n\right) - \frac{1}{2}\left(C_\rho^{n-1} - C_{W,C}^{n-1}\right). \tag{31}$$

S2. The diffusion term is integrated in M' fractional steps of size $\Delta t'$. The first step is performed using a second-order Runge–Kutta (RK2) scheme, using as starting values the known field values at time t_n. When $M' > 1$, the following $M' - 1$ fractional steps are performed using AB2. Each of the fractional steps accounts for half the explicit convection terms. Thus, the AB2 fractional steps take the form

$$\frac{(\rho Y_i)^{k+1} - (\rho Y_i)^k}{\Delta t'} = \frac{3}{2}D_i^k - \frac{1}{2}D_i^{k-1} + \frac{1}{2}C_i^e \tag{32}$$

$$\frac{\rho^{k+1} - \rho^k}{\Delta t'} = \frac{3}{2}\left(D_\rho^k - C_{W,D}^k\right) - \frac{1}{2}\left(D_\rho^{k-1} - C_{W,D}^{k-1}\right) + \frac{1}{2}S_\rho^e \tag{33}$$

$$T^{k+1} = \frac{P_0\bar{W}^{k+1}}{\rho^{k+1}}.$$

S3. The reaction source terms are integrated over a full time step Δt, using as starting values the computed scalar fields at the end of the previous step. We also account for half the explicit convection source terms and symbolically express the integration as

$$(\rho Y_i)^{s+1} - (\rho Y_i)^s = S\int_{\Delta t}\left[\mathrm{Da}\, w_i(\rho, T, \mathbf{Y}) + \frac{1}{2}C_i^e\right]dt \tag{34}$$

$$\rho^{s+1} - \rho^s = S\int_{\Delta t}\left[-\frac{1}{c_p T}\mathrm{Da}\, w_T - C_{W,R} + \frac{1}{2}S_\rho^e\right]dt \tag{35}$$

$$T^{s+1} = \frac{P_0\bar{W}^{s+1}}{\rho^{s+1}}. \tag{36}$$

S4. A convection–diffusion step identical to **S2** is performed. Specifically, the diffusion term is integrated in M' fractional steps of size $\Delta t'$, and each of these steps accounts for half the convection source term. The starting values are the scalar fields computed at the end of the previous step. **S4** results in intermediate values of the scalar fields, denoted by $(\tilde{\rho}, \tilde{\mathbf{Y}}, \tilde{T})$.

S5. Update the velocity field using the pressure-split momentum equations. The convective terms are treated explicitly using the second-order Adams–Bashforth scheme over a full time step, while the viscous terms are integrated in L fractional steps. The first fractional diffusion step is performed with RK2, using as starting values the known field quantities at t_n. The following $L - 1$ steps are performed with AB2. The convective source terms are accounted for within the fractional diffusion steps. Thus, the AB2 fractional steps take the form

$$\frac{(\rho\mathbf{v})^{l+1} - (\rho\mathbf{v})^l}{\Delta t''} = \frac{3}{2}\mathbf{F}(\mu^l, \mathbf{v}^l) - \frac{1}{2}\mathbf{F}(\mu^{l-1}, \mathbf{v}^{l-1}) + \mathbf{C}_v^e, \tag{37}$$

where

$$\mathbf{C}_v^e \equiv \frac{3}{2}\mathbf{N}^n - \frac{1}{2}\mathbf{N}^{n-1} \tag{38}$$

is the effective convection source term. The intermediate values of density and viscosity are obtained by interpolation between the values based on the predicted scalar fields and the known values at t_n; we set

$$\rho^l = \rho^n + \frac{l}{L}[\tilde{\rho} - \rho^n] \tag{39}$$

$$\mu^l = \mu(T^n) + \frac{l}{L}[\mu(\tilde{T}) - \mu(T^n)]. \tag{40}$$

The intermediate velocity field $\overline{\mathbf{v}} \equiv \mathbf{v}^L$ resulting from the above fractional step update is then corrected using the projection step

$$\frac{\tilde{\rho}\tilde{\mathbf{v}} - \tilde{\rho}\overline{\mathbf{v}}}{\Delta t} = -\nabla \tilde{p}, \tag{41}$$

where $\tilde{p}$ is the solution of (17).

Thus, at the end of **S5**, predicted values for both scalar fields, $(\tilde{\rho}, \tilde{\mathbf{Y}}, \tilde{T})$, and the velocity field, $\tilde{\mathbf{v}}$, are available.

3.2.2. *Non-stiff Corrector*

While a stiff corrector formulation is possible, as illustrated in the Appendix, it is important to note that the need for a corrector is dictated by the stability requirements for the variable-density projection scheme [73, 74] and not those of the scalar integration. In particular, the scalar integration in a stiff corrector formulation involves a repetition of the RK2/AB2 diffusion steps and the stiff integration of the reaction source terms done in the predictor, albeit with modified convective terms. This suggests that the convective change in the scalars is the only component of $\tilde{\rho} - \rho^n$ and $(\widetilde{\rho Y_i}) - (\rho Y_i)^n$ that requires correction. Based on this observation, a non-stiff corrector is formulated as follows.

S6. Effective convection source terms for species and density evolution equations are re-evaluated using an RK2 approach based on the starting values at t_n and the predicted values from **S5**. Thus, we set

$$C_i^* = \frac{1}{2}C_i(\tilde{\rho}, \tilde{\mathbf{v}}, \tilde{Y}_i) + \frac{1}{2}C_i^n \tag{42}$$

$$S_\rho^* = \frac{1}{2}[C_\rho(\tilde{\rho}, \tilde{\mathbf{v}}, \tilde{T}) - C_{W,C}(\tilde{\rho}, \tilde{\mathbf{v}}, \tilde{Y}_i)] + \frac{1}{2}\left(C_\rho^n - C_{W,C}^n\right). \tag{43}$$

S7. The effective non-convective change in the scalars in the predictor step is evaluated:

$$\Delta\rho \equiv \tilde{\rho} - \rho^n - \Delta t\left[\frac{3}{2}\left(C_\rho^n - C_{W,C}^n\right) - \frac{1}{2}\left(C_\rho^{n-1} - C_{W,C}^{n-1}\right)\right] \tag{44}$$

$$\Delta(\rho Y_i) \equiv (\widetilde{\rho Y_i}) - (\rho Y_i)^n - \Delta t\left[\frac{3}{2}C_i^n - \frac{1}{2}C_i^{n-1}\right]. \tag{45}$$

S8. The corrected scalar fields are evaluated:

$$\rho^{n+1} = \rho^n + \Delta\rho + \Delta t S_\rho^* \tag{46}$$

$$(\rho Y_i)^{n+1} = (\rho Y_i)^n + \Delta(\rho Y_i) + \Delta t C_i^* \tag{47}$$

$$T^{n+1} = \frac{P_0 \bar{W}^{n+1}}{\rho^{n+1}}. \tag{48}$$

Thus, **S8** results in the fully updated scalar fields $(\rho^{n+1}, \mathbf{Y}^{n+1}, T^{n+1})$.

S9. Update the velocity field using the pressure-split momentum equations. The procedure is very similar to that in **S5**, except that the intermediate scalar fields are based on interpolation between updated values at t_{n+1} and the starting values at t_n. Thus, in the corrector the AB2 fractional steps are given by

$$\frac{(\rho\mathbf{v})^{l+1} - (\rho\mathbf{v})^l}{\Delta t''} = \frac{3}{2}\mathbf{F}(\mu^l, \mathbf{v}^l) - \frac{1}{2}\mathbf{F}(\mu^{l-1}, \mathbf{v}^{l-1}) + \mathbf{C}_v^e, \tag{49}$$

where

$$\rho^l = \rho^n + \frac{l}{L}[\rho^{n+1} - \rho^n] \tag{50}$$

$$\mu^l = \mu(T^n) + \frac{l}{L}[\mu(T^{n+1}) - \mu(T^n)]. \tag{51}$$

The velocity distribution $\hat{\mathbf{v}} \equiv \mathbf{v}^L$ resulting from the above fractional step update is then corrected using the projection step

$$\frac{\rho^{n+1}\mathbf{v}^{n+1} - \rho^{n+1}\hat{\mathbf{v}}}{\Delta t} = -\nabla\hat{p}, \tag{52}$$

where $\hat{p}$ is the solution of (26).

S9 completes the integration cycle, as updated values for both the scalar fields, ρ^{n+1}, $\mathbf{Y}^{n+1}$, and T^{n+1}, and the velocity field, $\mathbf{v}^{n+1}$, are available.

4. SIMPLIFIED ANALYSIS

As described above, the present approach relies on multiple fractional times and combines a stiff integrator with linear multi-step and predictor–corrector methods. Consequently, a number of questions immediately arise regarding the construction. For instance, does the overall scheme in fact exhibit the expected second-order convergence? What is the effect of the number of fractional diffusion steps on the accuracy of integration? Furthermore, the stiff-integration procedure in DVODE [12] is based on achieving a desired accuracy by controlling the vector $\mathbf{e} = (e_1, e_2, \ldots, e_P)$ of estimated local errors in the solution $\mathbf{y} = (y_1, y_2, \ldots, y_P)$. The solver adaptively refines the internal time step and performs nonlinear Newton iterations so that the root-mean-square (rms) norm of the vector $\mathbf{q}$, $q_j \equiv e_j/m_j$, $j = 1, \ldots, P$, falls below 1, i.e.,

$$\left(\frac{1}{P}\sum_{j=1}^{P} q_j^2\right)^{1/2} \leq 1. \tag{53}$$

Here, $m_j \equiv r_j|y_j| + a_j$, $j = 1, \ldots, P$, is a vector of weights, while r_j and a_j are user-defined relative and absolute tolerances for the jth component of the solution, respectively. Since the accuracy of the stiff integration depends on these tolerances, how should they be selected and what is their effect on the overall behavior of the solution?

Due to the large number of parameters involved, and since repeated unsteady calculations with detailed kinetics are computationally expensive, we consider here a simplified setting that closely mimics the targeted simulations and that enables us to address the above questions in a detailed and efficient fashion.

4.1. Specification of the Simplified Problem

We consider the following family of nonlinear reaction–diffusion equations,

$$\frac{\partial u}{\partial t} = \frac{\partial^2 u}{\partial x^2} + \frac{8}{\delta^2} u^2(1-u), \qquad -\infty \le x \le \infty, \tag{54}$$

with boundary conditions $u(x) \to 1$ as $x \to -\infty$ and $u(x) \to 0$ as $x \to \infty$. Here, $\delta > 0$ is a freely selected parameter.

It is easy to verify that Eq. (54) admits the family of solutions

$$u(x,t) = \frac{1}{2}\left(1 - \tanh\left[\frac{x - ct}{\delta}\right]\right), \tag{55}$$

where $c = 2/\delta$.

In addition, it is natural to interpret the solution (55) as a steady-propagating front of width δ and speed c. Clearly, Eq. (54) has a structure similar to that of the scalar equations in the system for zero-Mach-number combustion. Together with the availability of exact solutions, this provides an ideal setting for analyzing the present split, stiff-integration approach.

Below, we adapt the scheme of the previous section to the simulation of Eq. (54). The simulations are initialized using the steady solutions given in Eq. (55); i.e., we set

$$u(x,0) = \frac{1}{2}\left(1 - \tanh\left[\frac{x}{\delta}\right]\right). \tag{56}$$

Solutions are obtained using a finite-difference grid which extends over the interval $-Z \le x \le Z$, $Z \gg \delta$. Second-order centered differences are used to approximate the diffusion term. At $x = -Z$, the Dirichlet condition $u(-Z,t) = 1$ is used, while a homogeneous Neumann condition is used at $x = Z$. The domain truncation length Z is selected large enough that the solution is essentially independent of both Z and the conditions imposed at the boundaries of the domain.

In order to analyze the behavior of the split stiff scheme, solutions are also obtained using a second-order non-split explicit scheme. The non-split scheme uses RK2 time integration as a startup procedure, and AB2 for subsequent time steps. For the split scheme with $M = 2$, the time step is naturally restricted by the RK2 diffusion stability limit, with the critical time step in 1D,

$$\Delta t_c \equiv \frac{\Delta x^2}{2}, \tag{57}$$

where Δx is the mesh size. Unless otherwise indicated, we will refer to this Δt_c below to imply $\Delta t_c(M=2)$ of the split scheme in 1D. Note that the corresponding critical time step for the explicit AB2 scheme in 1D is $\Delta x^2/4$.

4.2. Numerical Study

The results of the explicit calculations are compared to solutions obtained using the stiff, operator-split scheme. As outlined earlier (Eq. (28)), these solutions combine M explicit diffusion sub-steps, each of size $\Delta t' = \Delta t/M$, with a single stiff step, Δt, for the reaction source term. When comparing the results of split calculations, we fix $\Delta t'$ and vary M; thus, the global time step Δt is varied while the diffusion sub-step $\Delta t'$ is constant. Also, for the purposes of the analysis, the diffusion sub-step in the split computations coincides with the global time step of the explicit, non-split computations.

In most cases, we shall focus on a propagating front with width $\delta = 1$. Simulations are performed on a finite domain with $Z = 20$, with different resolution levels $\Delta x = 2Z/N$, where N is the total number of sub-intervals. Equation (54) is integrated to $t = 0.6144$; i.e., the front propagates for a distance approximately 1.2 times its own width. At the end of the computations, local errors are computed using the exact solution,

$$e_i^n = u_i^n - u_{\text{ex}}(x_i, t_n) = u_i^n - \frac{1}{2}\left(1 - \tanh\left[\frac{x_i - 2t_n/\delta}{\delta}\right]\right), \tag{58}$$

and a global error measure is formed using the discrete l_2 norm,

$$E_2 = \left[\frac{1}{N+1}\sum_{i=1}^{N+1}\left(u_i^n - u_{\text{ex}}(x_i, t_n)\right)^2\right]^{1/2}. \tag{59}$$

4.2.1. *Spatial and Temporal Errors*

Figure 1 shows the spatial distribution of the error at the end of the computations for a steady front with $\delta = 1$. Plotted are results obtained at three resolution levels, $N = 1000$, 2000, and 4000, and different values of M. The fractional diffusion sub-step is taken as half the (RK2) critical diffusion step, i.e., $\Delta t' = \Delta t_c/2 = \Delta x^2/4$. The stiff integration of the reaction term uses zero relative tolerance and an absolute tolerance of 10^{-13}. Also shown in Fig. 1 are results obtained with a non-split AB2 scheme with $\Delta t = \Delta x^2/4$. For the cases of Fig. 1, Table I shows the corresponding rms errors, together with the temporal order of convergence of the calculations. The latter is obtained by repeating the calculations with decreasing time steps and monitoring the differences between numerical solutions obtained at the same spatial resolution level. This enables us to isolate time discretization errors and consequently determine the temporal order of convergence.

Figure 1 and Table I show that for $N = 4000$ the spatial error distribution and the rms values are essentially independent of M, at least in the range considered. For $N = 2000$, the errors remain essentially constant as long as $M \leq 32$, while for $N = 1000$ errors are nearly constant when $M \leq 16$. Meanwhile, Table II shows that for $N = 1000$, the rms error at the final time is essentially independent of the time step, except for slight changes for $M = 32$ for the largest time step considered, $\Delta t' = \Delta t_c/2$. Combined, the results of Fig. 1 and Tables I and II lead to the following two observations: (1) The rms errors at the final time are essentially independent of both M and $\Delta t'$, as long as the global time step

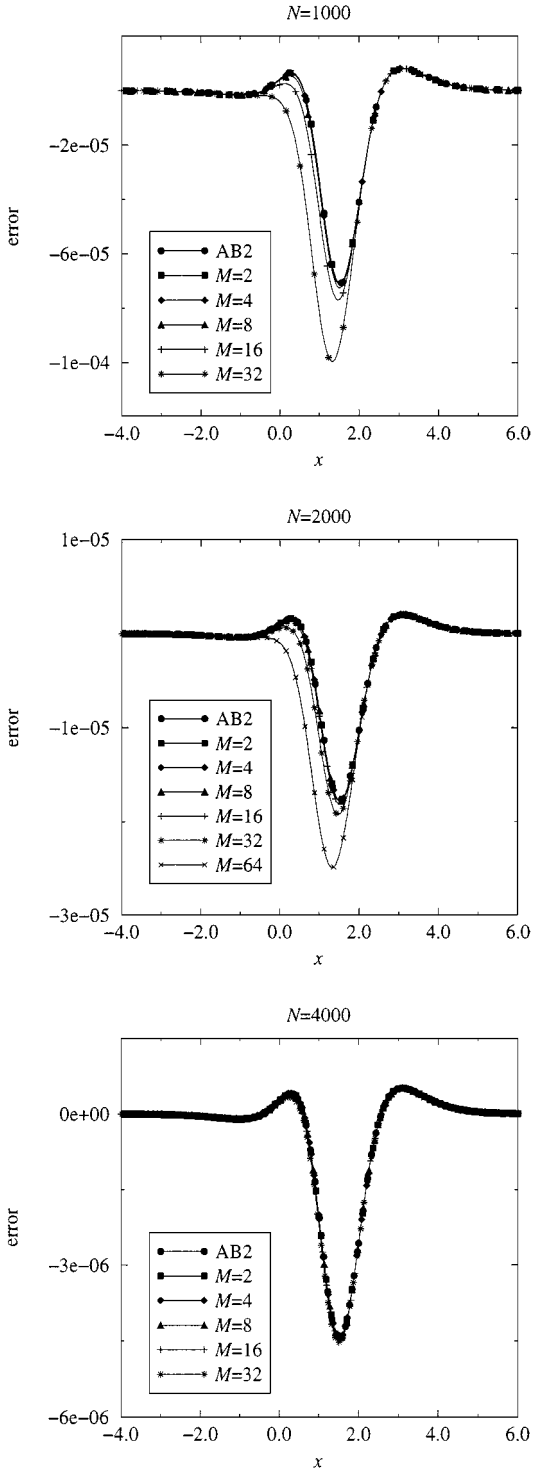

FIG. 1. Spatial distribution of the error between the numerical and exact solutions for the split scheme with different values of M. Results using an explicit non-split AB2 scheme are also plotted. The absolute and relative tolerances used are 10^{-13} and 0, respectively. The computations are performed with $\delta = 1$, $Z = 20$, and $N = 1000$ (top), $N = 2000$ (middle), and $N = 4000$ (bottom). The fractional diffusion step $\Delta t' = t_c/2$.

TABLE I
Root-Mean-Square Error and Order of Convergence for Reacting Front Simulations with $\delta = 1$, $Z = 20$, and $\Delta t' = \Delta t_c/2$

Scheme	$\Delta t' \times 10^4$	$\Delta t \times 10^4$	rms error $\times 10^6$	Order of convergence
		$N = 1000$, $\Delta x = 0.04$		
AB2	—	4	9.9379	1.9994
Split, $M = 2$	4	8	9.9711	1.9929
Split, $M = 4$	4	16	10.025	1.9988
Split, $M = 8$	4	32	10.222	1.9998
Split, $M = 16$	4	64	11.063	1.9999
Split, $M = 32$	4	128	15.111	1.9999
		$N = 2000$, $\Delta x = 0.02$		
AB2	—	1	2.4864	1.9998
Split, $M = 2$	1	2	2.4883	1.4347
Split, $M = 4$	1	4	2.4917	1.9208
Split, $M = 8$	1	8	2.5038	1.9925
Split, $M = 16$	1	16	2.5525	1.9986
Split, $M = 32$	1	32	2.7626	1.9997
Split, $M = 64$	1	64	3.7757	1.9999
		$N = 4000$, $\Delta x = 0.01$		
AB2	—	0.25	0.62176	1.9999
Split, $M = 2$	0.25	0.50	0.62145	−0.5411
Split, $M = 4$	0.25	1.0	0.62187	0.1183
Split, $M = 8$	0.25	2.0	0.62273	1.3625
Split, $M = 16$	0.25	4.0	0.62576	1.9184
Split, $M = 32$	0.25	8.0	0.63793	1.9926

Note. The split scheme uses an absolute tolerance of 10^{-13}.

$\Delta t = M\Delta t'$ falls below a well-defined value. This value appears to be weakly dependent on the spatial resolution level. (2) When the global time step is sufficiently small (in the sense just described) the rms errors are dominated by the spatial discretization errors. This can be appreciated from Table II. Note that the dominant effect of the spatial discretization error complicates the temporal convergence analysis, which, as mentioned above, requires that one carefully isolate spatial and temporal errors.

TABLE II
Root-Mean-Square Errors for Reacting Front Simulations with $\delta = 1$, $Z = 20$, and $N = 1000$

Scheme	$\Delta t' = \Delta t_c/2$	$\Delta t' = \Delta t_c/4$	$\Delta t' = \Delta t_c/8$
AB2 ($\Delta t = \Delta t'$)	9.9379×10^{-6}	9.9445×10^{-6}	9.9461×10^{-6}
Split, $M = 2$	9.9711×10^{-6}	9.9527×10^{-6}	9.9481×10^{-6}
Split, $M = 4$	10.025×10^{-6}	9.9662×10^{-6}	9.9515×10^{-6}
Split, $M = 8$	10.222×10^{-6}	10.014×10^{-6}	9.9635×10^{-6}
Split, $M = 16$	11.063×10^{-6}	10.208×10^{-6}	10.011×10^{-6}
Split, $M = 32$	15.111×10^{-6}	11.048×10^{-6}	10.205×10^{-6}

Note. The split calculations use an absolute tolerance of 10^{-13}.

4.2.2. *Convergence Rate*

Table I also indicates that the split time integration does achieve second-order convergence. Second-order convergence is in fact observed in all cases considered, except for $N = 4000$, where the global time step Δt is very small. (Recall that in Table I, $\Delta t = M\Delta t_c/2$, and that the critical diffusion step Δt_c varies as Δx^2.) Specifically, for $N = 4000$ the computed order of convergence increases monotonically from a negative value at $M = 2$ to approximately 2 at $M = 32$.

Detailed analysis of the computations reveals that the origin of this phenomenon is associated with the *relative* magnitude of the stiff-integration errors with respect to errors associated with the fractional integration of the diffusion time step. As mentioned earlier, DVODE uses absolute and relative tolerances to control the integration error; for simplicity the present tests use zero relative tolerance and an absolute tolerance of 10^{-13}. Meanwhile, in the multi-step methods used to treat the diffusion term, integration errors are proportional to $\Delta t'^2$. Thus, one would expect the global time integration error to behave as the sum of two terms: a constant that depends on the tolerances of the stiff integrator, and an $O(\Delta t'^2)$ contribution due to the integration of the diffusion term. When the selected tolerances are such that the stiff-integration errors are significantly smaller than the explicit $O(\Delta t'^2)$ errors, one would obviously expect the scheme to exhibit second-order convergence. This is consistent with the results obtained for $N = 1000$, for $N = 2000$ with $M \geq 4$, and for $N = 4000$ when $M \geq 16$. On the other hand, when the stiff-integration errors are comparable with the remaining (second-order) errors, one would expect time convergence tests to yield an order of convergence that is lower than 2. This trend is observed in Table I for $N = 2000$ and $M = 2$ and for $N = 4000$ and $M = 8$. Finally, when the stiff-integration errors are dominant, the global time-integration error should essentially be independent of diffusion step, and the convergence analysis is expected to yield approximately zero-order convergence. This behavior can be seen in Table I for $N = 4000$ and $M \leq 4$.

4.2.3. *Stiff-Integration Error Tolerances*

In order to further examine the above trends, additional tests were conducted to analyze the effect of the tolerances used in the stiff integrator. A sample of these computations is provided in Table III, which provides rms errors obtained with $N = 1000$ and absolute tolerances of 10^{-12} and 10^{-11}. The results of Table III are consistent with our observations above. In particular, they show that increasing the tolerance may lead to a reduction in the computed order of convergence, and that increasing M (and consequently Δt) at a fixed tolerance level leads to an increase in the computed order of convergence! This is because the stiff-integration errors are controlled by the user-defined tolerance level, while the errors due to splitting and explicit treatment of diffusion vary quadratically with Δt. Thus, by fixing the tolerance and increasing the global time step, the relative magnitude of stiff-integration errors decreases. (One should also note that increasing the integration interval at a fixed tolerance level places a heavier burden on the stiff integration, which must deliver the same accuracy for a larger integration period.) Another interesting observation in Tables I and III is that while the tolerance value may have a significant effect on the computed order of convergence, its effect on the rms error value appears to be insignificant. In fact, the results clearly show that, for all the tolerances considered, spatial discretization errors remain dominant, as long as the global time step remains small.

TABLE III

Effect of Absolute Tolerance on rms and Order of Convergence for Reacting Front Simulations with $\delta = 1$, $Z = 20$, $N = 1000$, and $\Delta t' = \Delta t_c/2$

Scheme	rms error $\times 10^6$	Order of convergence
	Absolute tolerance $= 10^{-12}$	
Split, $M = 2$	9.9708	1.9087
Split, $M = 4$	10.025	1.9907
Split, $M = 8$	10.222	1.9983
Split, $M = 16$	11.063	1.9997
Split, $M = 32$	15.111	1.9999
	Absolute tolerance $= 10^{-11}$	
Split, $M = 2$	9.9680	1.2753
Split, $M = 4$	10.023	1.8961
Split, $M = 8$	10.221	1.9915
Split, $M = 16$	11.063	1.9971
Split, $M = 32$	15.111	1.9994

4.2.4. *Splitting Errors*

In order to further analyze the performance of the split scheme, tests were also performed to determine an approximate criterion for splitting errors to become significant. Intuitively, one would expect splitting errors to remain small as long as the changes during a complete integration step are relatively small. For the present reaction–diffusion problem, a reasonable interpretation is that the characteristic diffusion depth during a time step, ℓ, is much smaller than the width of the front, i.e., $\ell \sim \sqrt{\Delta t} < a\delta$ with $a \ll 1$.

From Table I, one observes that rms errors are essentially independent of Δt as long as $M \leq 16$, i.e., $a \sim 0.04$. In order to verify this approximate scaling, computations were performed for a thin reaction–diffusion front with $\delta = 0.5$, using $Z = 10$ and $N = 1000$, and were carried to a final time $t_f = 0.3122$; i.e., the ratio of front propagation distance to front width is equal to that of the earlier case with $\delta = 1$. The computed errors for different values of M are reported in Table IV. Note that the thin front runs are performed with $\Delta t' = 10^{-4}$; i.e., the ratio ℓ/δ for a given value of M is the same in Table I (with $N = 1000$) and Table IV.

TABLE IV

Root-Mean-Square Error and Order of Convergence for Reacting Front Simulations with $\delta = 0.5$, $Z = 10$, $N = 1000$, $\Delta x = 0.02$, and $\Delta t' = 10^{-4}$

Scheme	rms error $\times 10^6$	Order of convergence
Split, $M = 2$	9.9711	1.9929
Split, $M = 4$	10.025	1.9988
Split, $M = 8$	10.222	1.9998
Split, $M = 16$	11.063	1.9999
Split, $M = 32$	15.111	1.9999

Note. An absolute tolerance of 10^{-13} is used.

These tables show that the rms errors for the thin and thick fronts are nearly identical. This behavior is consistent with the above intuitive scaling.

These results suggest that, in the present setting, the global time step can be based approximately on $\Delta t \sim 16 \times 10^{-4}\delta^2$; accordingly the number of fractional diffusion steps follows $M \equiv \Delta t/\Delta t' \sim 16 \times 10^{-4}\delta^2/(\Delta x^2/4) = 64 \times 10^{-4}(\delta/\Delta x)^2$. This scaling is only approximate, as a weak dependence on spatial resolution can be seen in Table I. Nonetheless, it still suggests that, for a given front width δ, M can be increased as the front resolution is increased. Moreover, with the time scale for front propagation $\delta t_f = \delta/c = \delta^2/2$, the above scaling translates to $\Delta t \sim 0.0032\delta t_f$, such that the time step is a small fraction of the physical time scale of the flow.

4.2.5. *Summary Remarks*

One should note that, since the stiff integration generally dominates the CPU time in detailed kinetics applications, the selection of appropriate tolerance levels plays a crucial role in the overall efficiency of the calculation. The experiences above provide approximate but useful guidelines for the selection of both the integration step (or equivalently the number of fractional diffusion steps) and the tolerance levels. In particular, the analysis shows that:

1. When the tolerance level is small, the operator-split, stiff scheme achieves second-order convergence, as the overall temporal error is dominated by the operator-splitting and explicit error contributions.
2. By increasing the number of fractional diffusion steps, and consequently the global time step, the tolerances used in the stiff integrator can be accordingly increased.
3. When the tolerance levels are increased, the computed order of convergence of the scheme may start decreasing. One can use this phenomenon as an initial guideline for the selection of an adequate tolerance level, but this approach may yield an overly conservative estimate. A more suitable approach for the selection of both the number of fractional steps and the tolerance level is to monitor the behavior of the solution error, as the latter is often dominated by the spatial error.
4. A simple guideline for selecting the number of fractional steps is that the global time step should remain significantly smaller than the physical time scales of the problem. It also appears that this initial guess can be made independently of the selected spatial resolution level.

4.3. Alternative Splitting Procedures

We conclude this section with a brief discussion of two variants of the above splitting procedure, as applied to the present simplified problem. In the first variant, the splitting is performed in an alternating fashion, with M fractional diffusion steps followed by a stiff fractional reaction step at odd time steps and a stiff fractional reaction step followed by M fractional diffusion steps at even time steps. Following the notation above, this alternating scheme is represented as

$$U^{n+1} = \begin{cases} \mathcal{D}^M_{\Delta t'}\mathcal{S}_{\Delta t}U^n, & n \text{ even} \\ \mathcal{S}_{\Delta t}\mathcal{D}^M_{\Delta t'}U^n, & n \text{ odd.} \end{cases} \tag{60}$$

Thus, while the splitting is not symmetric within a single time step, symmetry is maintained

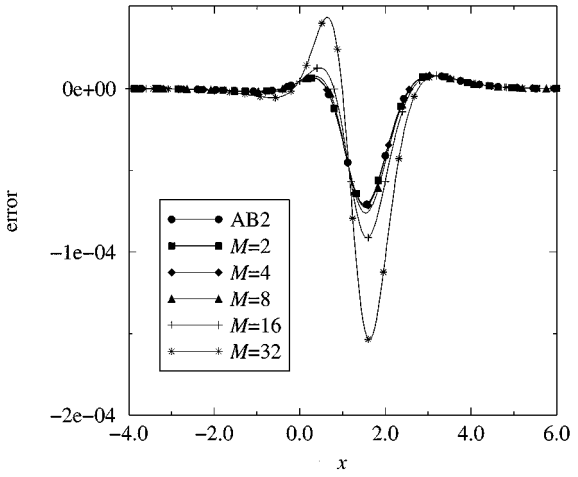

FIG. 2. Spatial distribution of the error between the numerical and exact solutions for an alternating split scheme with different values of M. Results using an explicit non-split AB2 scheme are also plotted. The absolute and relative tolerances used are 10^{-13} and 0, respectively. The computations are performed with $\delta = 1$, $Z = 20$, and $N = 1000$. The fractional diffusion step $\Delta t' = t_c/2$.

for a pair of consecutive steps. Accordingly, global second-order time convergence is still expected.

To examine the behavior of the alternating scheme, computational tests were conducted using the same approach followed above. A representative sample of the results is provided in Fig. 2, which shows the spatial distribution of errors at the end of the calculation for a front with $\delta = 1$. For the same case, rms errors at the end of the calculations are reported in Table V. Briefly, our experiences with the alternating scheme have been very similar to those with the symmetric scheme. In particular, the results clearly show that second-order temporal convergence can in fact be achieved. The general similarity between the results of the alternating scheme (Fig. 2 and Table V) and the corresponding results of the symmetric calculations (Fig. 1 and Table I) is also evident. However, one notes that while the errors in the alternating and symmetric schemes are comparable at low Δt, the errors in the alternating scheme become noticeably higher as the time step increases. A related observation is that the operator-split results start deviating from the AB2 predictions at

TABLE V

Root-Mean-Square Error and Order of Convergence for Reacting Front Simulations with $\delta = 1$, $Z = 20$, $N = 1000$, $\Delta x = 0.04$, and $\Delta t' = 4 \times 10^{-4}$

Scheme	rms error $\times 10^6$	Order of convergence
Split, $M = 2$	9.9967	1.9950
Split, $M = 4$	10.104	1.9991
Split, $M = 8$	10.538	1.9998
Split, $M = 16$	12.352	1.9996
Split, $M = 32$	20.524	1.9987

Note. An alternating split scheme with an absolute tolerance of 10^{-13} is used.

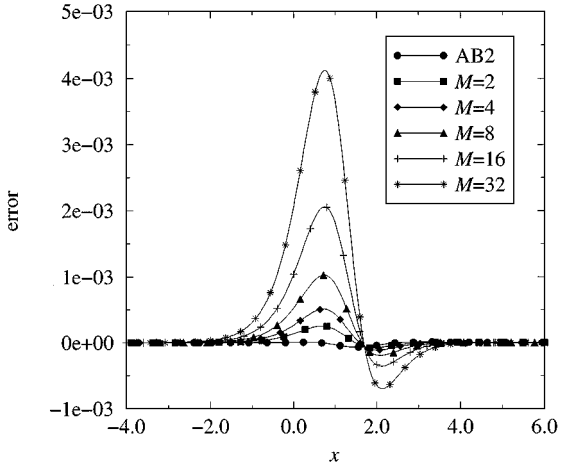

FIG. 3. Spatial distribution of the error between the numerical and exact solutions for an asymmetric split scheme with different values of M. Results using an explicit non-split AB2 scheme are also plotted. The absolute and relative tolerances used are 10^{-13} and 0, respectively. The computations are performed with $\delta = 1$, $Z = 20$, and $N = 1000$. The fractional diffusion step $\Delta t' = t_c/2$.

values of M in the alternating scheme (Fig. 2) lower than those in the symmetric scheme (Fig. 1). These trends can also be appreciated by comparing the results of Tables I and V, especially at higher values of Δt.

Finally, we consider an asymmetric split scheme in which integration of the diffusion term is performed first, followed by stiff integration of the reaction term. Thus, the time integration is expressed as

$$U^{n+1} = \mathcal{S}_{\Delta t} \mathcal{D}^M_{\Delta t'} U^n. \tag{61}$$

The asymmetric scheme is also applied to computing the steady propagation of a front with $\delta = 1$, and the results are used to analyze the temporal behavior of the computations. Figure 3 shows the spatial distribution of errors at the end of the simulation; the corresponding rms error values are reported in Table VI. The results clearly show that the asymmetric split scheme is first order in time. In contrast with the results for the symmetric and alternating schemes, the computations indicate that the (first-order) time-integration errors in

TABLE VI

Root-Mean-Square Error and Order of Convergence for Reacting Front Simulations with $\delta = 1$, $Z = 20$, $N = 1000$, $\Delta x = 0.04$, and $\Delta t' = 4 \times 10^{-4}$

Scheme	rms error $\times 10^5$	Order of convergence
Split, $M = 2$	3.9570	0.9994
Split, $M = 4$	8.0068	0.9990
Split, $M = 8$	16.188	0.9982
Split, $M = 16$	32.557	0.9966
Split, $M = 32$	65.166	0.9933

Note. An asymmetric split scheme is used with an absolute tolerance of 10^{-13}.

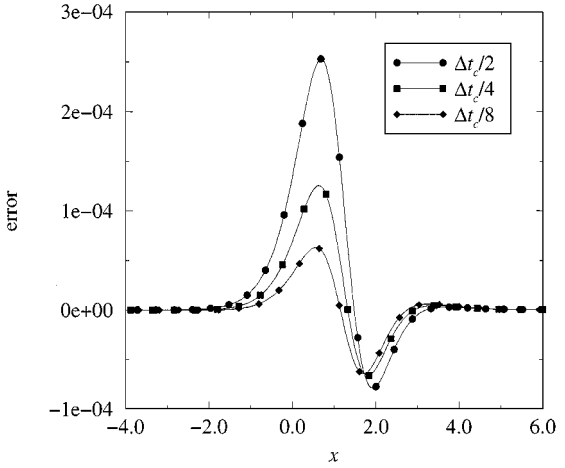

FIG. 4. Effect of the fractional diffusion step on the error for an asymmetric split scheme with $M = 2$. The absolute and relative tolerances used are 10^{-13} and 0, respectively. The computations are performed with $\delta = 1$, $Z = 20$, and $N = 1000$.

the asymmetric scheme are dominant. Furthermore, for the same choice of discretization parameters, Tables I, V, and VI show that the rms error in the asymmetric scheme is roughly an order of magnitude larger than the errors in the symmetric and alternating constructions.

The first-order behavior of the asymmetric computations is also analyzed in Fig. 4 and Table VII, which illustrate the effect of changing the time step at a fixed number of fractional diffusion steps, $M = 2$. These computations show that in order to reduce the error of the asymmetric calculations to levels comparable with those obtained with AB2, the *global* time step value must fall significantly below the critical diffusion limit. Consequently, it appears that for the present class of reaction–diffusion problems the asymmetric first-order splitting can only provide computational advantages at the expense of a significant drop in overall accuracy.

It should be emphasized that the above discussion ignores the CPU-time cost of the stiff integration procedure, and its dependence on the associated step size. Thus, the optimization of the parameters of the split, stiff scheme should not be simply based on the precision of the calculations. This aspect will be further discussed in the following section, in the (more practical) context of a detailed kinetics simulation.

TABLE VII
Effect of Time Step on the rms Error in Reacting Front Simulations with $\delta = 1$, $Z = 20$, $N = 1000$, and $\Delta x = 0.04$

Scheme	$\Delta t' = t_c/2$	$\Delta t' = t_c/4$	$\Delta t' = t_c/8$
Split, $M = 2$	3.9570×10^{-5}	2.0238×10^{-5}	1.2186×10^{-5}
Split, $M = 4$	8.0068×10^{-5}	3.9570×10^{-5}	2.023×10^{-5}
Split, $M = 8$	16.188×10^{-5}	8.0070×10^{-5}	3.9570×10^{-5}
Split, $M = 16$	32.557×10^{-5}	16.188×10^{-5}	8.0071×10^{-5}
Split, $M = 32$	65.166×10^{-5}	32.557×10^{-5}	16.188×10^{-5}

Note. An asymmetric split scheme with an absolute tolerance of 10^{-13} is used.

5. APPLICATION TO FLAMES WITH DETAILED KINETICS

We now present results for both 1D and 2D flames using stiff detailed kinetics. The 1D flame results are utilized to further examine the accuracy and convergence of the numerical scheme, while the 2D flame serves to demonstrate the capabilities and efficiency of the scheme. We use the GRImech1.2 [3] C_1C_2 chemical mechanism (32 species and 177 reactions) for methane–air combustion, and consider a stoichiometric 20% N_2-diluted premixed methane–air flame at atmospheric pressure, with reactants at ambient temperature, in an open domain.

5.1. 1D flame

A freely propagating premixed methane–air flame with the above composition and chemical mechanism is computed using Chemkin [64, 76] in 1D. This solution is interpolated onto a uniform 1D grid and used to initialize the computations. The initial flame structure is shown in Fig. 5. The computational domain is 1.6 cm long with inflow and outflow boundary conditions. Temperature and both reactant and product mole fractions are shown. The flame burns to the left into the reactants, which flow from left to right, with an inlet velocity of 19 cm/s at the left boundary, equal to the burning speed. The flow exhibits an initial unsteady phase as the flame structure, position, and reaction rates adjust to the spatial grid discretization and transport coefficients used in the present code, which are different from those in Chemkin. The flow evolution is studied to evaluate the numerical scheme.

5.1.1. *Convergence Rate*

We begin by examining the empirically observed order of convergence of the scheme in the global time step Δt. We look at both self-convergence of the split scheme, and its cross-convergence relative to the original non-split construction as Δt is reduced. This uses the rms measures, for any field quantity ϕ, at a given time, $\epsilon^{\text{self}}_{\Delta t} = \|\phi^{\text{split}}_{\Delta t} - \phi^{\text{split}}_{\Delta t/2}\|$, and $\epsilon^{\text{cross}}_{\Delta t} = \|\phi^{\text{split}}_{\Delta t} - \phi^{\text{non-split}}_{\Delta t}\|$. The cross-convergence results, shown in Fig. 6, indicate that the

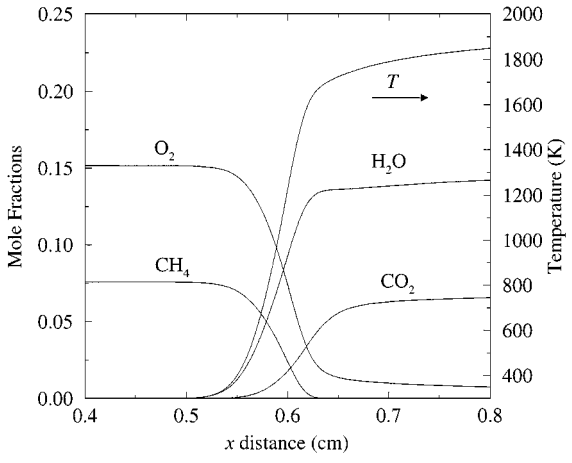

FIG. 5. One-dimensional stoichiometric 20% N_2-diluted premixed methane–air flame structure. Ambient temperature reactants are on the left, and hot combustion products are on the right. The GRImech1.2 [3] kinetic mechanism is used to model flame chemistry. For clarity, intermediate species are not shown.

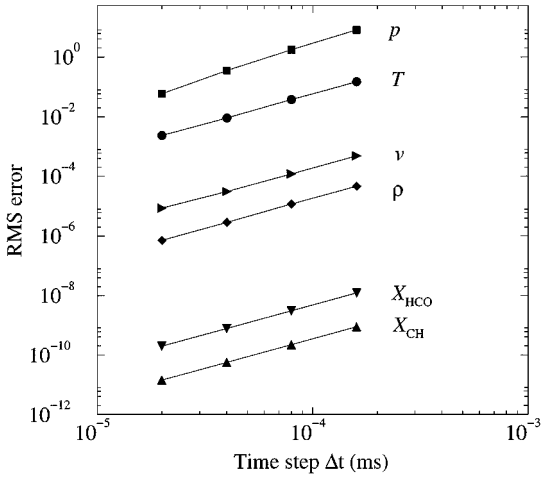

FIG. 6. Convergence of the rms error between 1D flame solutions with successive global time-step refinements, at $t = 0.15$ ms. The "error" reported here is the difference between the split and non-split scheme results. Absolute and relative error tolerances in the stiff-integration procedure for both schemes are 10^{-8} and 10^{-14}, respectively. The split-scheme results are based on $M = 16$, and $L = 4$.

computed solutions with the two schemes converge at a rate that is indeed second order in Δt. Similarly, the self-convergence of the split scheme is found to be $\mathcal{O}(\Delta t^2)$.

5.1.2. *Splitting Errors*

In order to further examine the rms errors, we integrate the 1D flow using a range of $M = \{2, 4, 8, 16, 32\}$, with a fixed $\Delta t = 50$ ns, $N = 512$ cells over the domain length, and with no viscous momentum splitting. The resulting computed solutions with the split scheme are compared against the non-split results (integrated with the same Δt). This is done for DVODE relative tolerance threshold values of $R = 10^{-5}$, 10^{-6}, and 10^{-8}, for all scalars. We also set the absolute tolerance threshold for each scalar quantity ϕ using $a_\phi = \phi_{\max} R$, where $\phi_{\max}$ is the maximum value of ϕ ($\phi > 0$) over the computational domain. The relative rms error results (normalized by the maximum value of each field quantity) are shown in Fig. 7, using the velocity, temperature, and CH mole fraction fields for illustration. Note first the negligible dependence of the error on M for all the fields shown. In fact, a small drop in error with higher M can be observed (for the T field, for example), which may be related to the reduction in the $\mathcal{O}(\Delta t'^2)$ error in the integration of the diffusion terms, as $\Delta t' = \Delta t / M$. Note that the flame thermal thickness is 0.069 cm, and the burning speed is 19 cm/s, resulting in a flame time scale of $t_f = 3.6$ ms. Thus, $\Delta t / t_f = 0.000014$, a very small fraction. It is not surprising therefore that the splitting errors are negligible, consistent with the simplified analysis in the previous section (small splitting errors have also been reported in [47]). On the other hand, the figure reveals strong dependence of the error on R for the velocity and temperature fields. Even though the same R is used for the split and non-split solutions in each case, the stiff-integration errors do not cancel due to the differences in the two time-integration schemes. Evidently, these errors are a significant component of the overall time-integration errors in this case for the v and T fields, but not for the CH mole fraction, where R is seen to have no effect on the error.

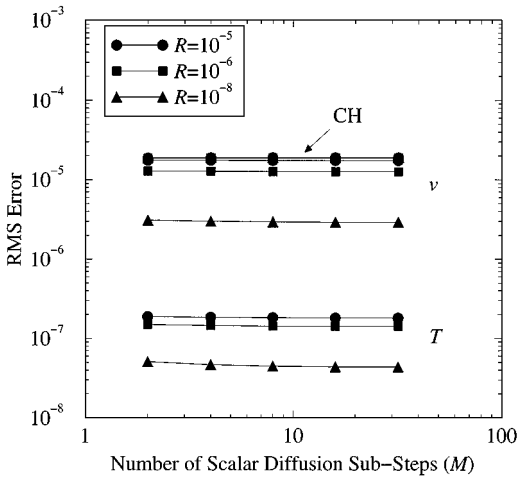

FIG. 7. Root-mean-square error results for the 1D detailed-chemistry flame. The flame is computed using $N = 512$ grid cells on a 1.6 cm domain, with a global time step of $\Delta t = 50$ ns and the indicated ranges of relative tolerance threshold R and number of scalar diffusion sub-steps M. No splitting of the viscous momentum terms is utilized. The error shown is the relative rms difference between the computed fields shown and those computed with the same spatial resolution and time step but with no scalar-diffusion splitting (normalized with the maximum value of each flow quantity). The error shows little dependence on the number of sub-steps, and significant dependence on R.

Figure 8 illustrates the effect of L, the number of viscous momentum sub-steps, on the rms error. For all cases, $\Delta t = 50$ ns and $N = 512$, as in Fig. 7. On the other hand, we now vary $\Delta t''$ with $L = \{2, 4, 8, 16, 32\}$ and use a fixed $M = 2$. The relative rms error is computed with respect to the non-split case with the same spatial resolution and global time step. As in Fig. 7, we see the minor role of splitting errors relative to the stiff-integration errors. This is clear from the effective independence of rms error on L. The dependence on R is evident, however, and is similar to that observed in Fig. 7.

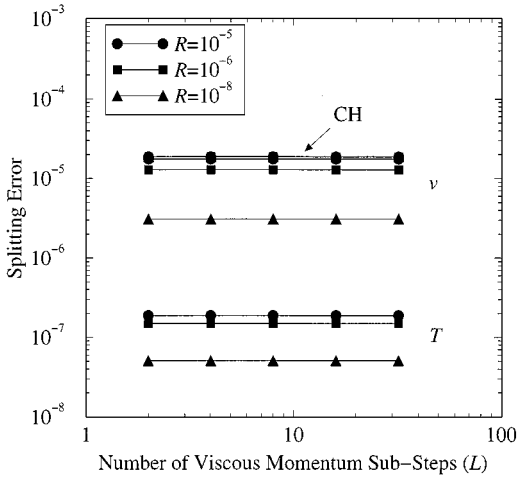

FIG. 8. Splitting errors and their dependence on the number of viscous momentum sub-steps L. This is the same fixed-Δt 1D flame case as that in Fig. 7, but with fixed $M = 2$ and L varying over the range indicated. Here again, the error shows little dependence on the number of sub-steps, and significant dependence on R.

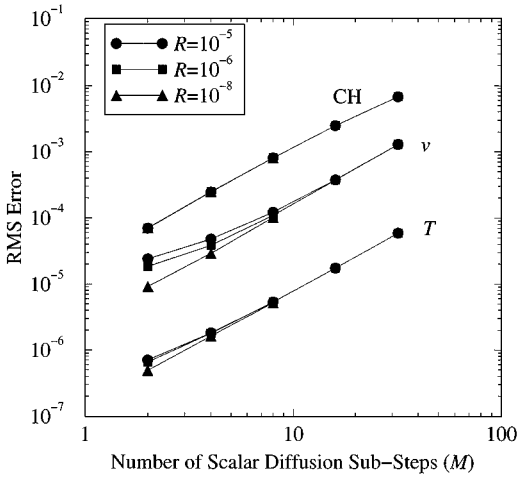

FIG. 9. Root-mean-square error results for the 1D detailed-chemistry flame. The flame is computed using $N = 512$ grid cells on a 1.6 cm domain, with a fixed scalar-diffusion sub-step of $\Delta t' = 50$ ns, and the indicated ranges of relative tolerance threshold R and number of scalar-diffusion sub-steps M. No splitting of the viscous momentum terms is utiized. The error shown is the relative rms difference between the computed fields shown and those computed with the same spatial resolution and time step but with no scalar-diffusion splitting. The error shows strong second-order dependence on the number of sub-steps M since $\Delta t = M\Delta t'$. At low $(M, \Delta t)$, R is found to have a significant effect on the error, as explicit time-integration errors become smaller than the stiff-integration errors.

5.1.3. *Temporal Discretization Errors and Stiff-Integration Tolerances*

In Figs. 9 and 10 we allow Δt to vary with M, while keeping $\Delta t'$ fixed, which is a more realistic situation. In Fig. 9, $\Delta t' = 50$ ns is large, such that we observe the second-order rise of the errors (defined with respect to the non-split case) as $(M, \Delta t)$ are increased. We also observe the role of stiff-integration tolerances which degrade the second-order behavior of

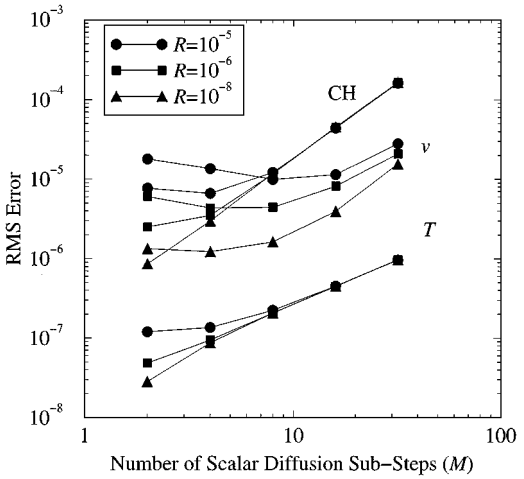

FIG. 10. Root-mean-square error results for the 1D detailed-chemistry flame. All conditions are similar to those in Fig. 9, except that a smaller $\Delta t' = 5$ ns, and associated $\Delta t = M\Delta t'$, is used here. In the present case, stiff-integration errors dominate the small-Δt explicit integration errors. This is evidenced by the observed strong role of R in modifying the rms error dependence on $(M, \Delta t)$.

the error at low $(M, \Delta t)$, as observed in Section 4. As expected from the model problem results, these effects are more pronounced in Fig. 10, with a smaller $\Delta t' = 5$ ns and associated smaller Δt. The fixed stiff-integration tolerances limit the reduction in error significantly at low $(M, \Delta t)$. Moreover, the uniformly observed second-order convergence rate in Fig. 9 is absent in Fig. 10. Only the CH mole fraction exhibits second-order convergence at large M, while degrading at small M for the high-R cases. For $R = 10^{-8}$ uniform second-order convergence is evident in the CH data. The v field convergence rate is seen to be much more influenced by the stiff-integration tolerances, with lower error and better convergence observed at low R and high $(M, \Delta t)$. The temperature field, on the other hand, approaches second-order convergence only for the $R = 10^{-8}$ case at *low* $(M, \Delta t)$. We also note, in reference to the CH and T data at low $(M, \Delta t)$ in Fig. 10, that the two-orders-of-magnitude change in R from 10^{-8} to 10^{-6} has a smaller influence on the rms error than the order-of-magnitude change from 10^{-6} to 10^{-5}. The corresponding changes in the v-data are of the same order. Both observations suggest that the error is more sensitive to the stiff-integration tolerance at large tolerance values. This makes sense, since the stiff-integration component of the rms error is expected to be more significant at large R. It is also consistent with the similar experience in [42]. This observation is not evident however in Fig. 9, which may be expected since the stiff-integration errors are not dominant in that case.

5.1.4. *Spatial Discretization Errors*

In Fig. 11, we report rms errors for fixed $\Delta t = 5$ ns, between split solutions with $N = 512$ grid cells in the 1D domain, and non-split solutions with $N = 2048$ cells. The factor of 4 change in Δx results in rms differences between the two computed solutions that include spatial discretization errors. The $M = 1$ data point in the figure corresponds to the non-split $N = 512$ solution. The general level of the error in Fig. 11 is higher by roughly two orders of magnitude than that in Fig. 7, despite the fact that the time step is smaller by a factor of 10. This increase is evidently due to the spatial discretization errors, which now seem to dominate over the stiff-integration and splitting errors, as there is little observed dependence

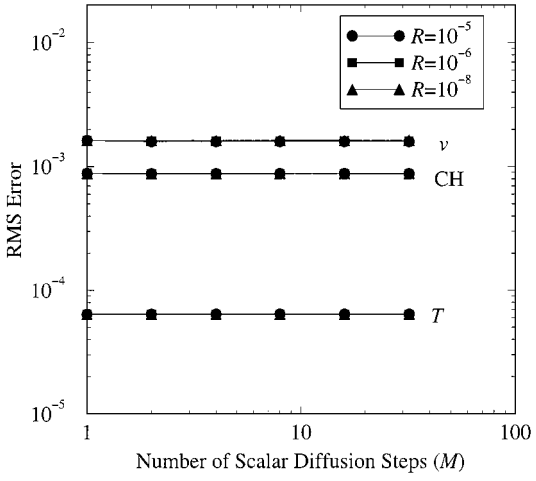

FIG. 11. Root-mean-square errors corresponding to the same $N = 512$ data in Fig. 7, but as compared to the non-split solution using $N = 2048$ albeit with the same Δt. This comparison brings in the spatial discretization errors, resulting in the observed general rise in the error as compared to Fig. 7, and the relative insensitivity to R, resulting from the dominance of spatial errors over stiff-integration errors.

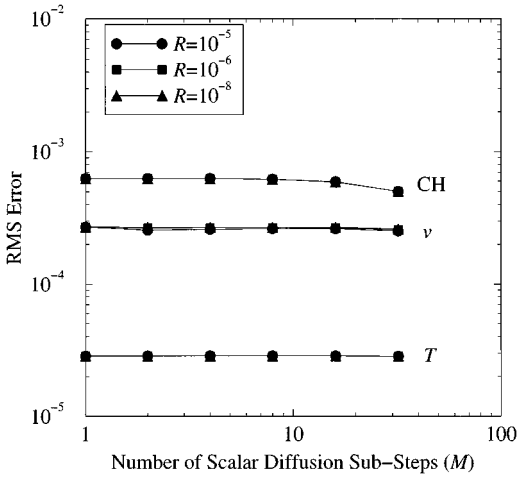

FIG. 12. Root-mean-square errors for the 1D detailed-chemistry flame, comparing the $N = 512$, $L = 0$, $M = \{0, 2, 4, 8, 16, 32\}$, $\Delta t' = 5$ ns case with the fine spatial resolution case using $N = 2048$, $L = 0$, $M = 0$, $\Delta t = \Delta t' = 5$ ns. Thus the rms error involves both spatial and temporal discretization errors, as in Fig. 11, although here Δt is increased with M. Note the relative insignificance of M, Δt, or R on the amplitude of the error, which is evidently dominated by spatial errors.

of the error on either M or R. This independence of R due to dominance of spatial errors is consistent with that observed in Section 4 above.

We also examine the spatial errors for fixed $\Delta t'$, and variable $(M, \Delta t)$. The data of Fig. 10, with $\Delta t' = 5$ ns and $N = 512$, are compared to the data of the non-split case with $N = 2048$ and $\Delta t = 5$ ns. The dependence of the resulting rms error on M, Δt, and R is shown in Fig. 12. These results show that the significant dependence of the rms error on R and $(M, \Delta t)$ observed in Fig. 10 is now entirely dominated by the spatial discretization errors. Again, this independence of R is consistent with the observations in Section 4 above. On the other hand, Fig. 12 reveals a slight decrease in the rms error with $(M, \Delta t)$, in contrast with the model problem results in Tables I and III. It is useful to recall, however, that the interpretation of this error measure is complicated by the fact that it is the rms difference between two fields, each of which has given truncation errors with respect to the exact solution. Thus, the actual dependence of the resulting quantity on finite Δt, M, L, R, and Δx is a complicated function whose behavior is only interesting insofar as the order of the leading terms in the limit as $(\Delta x, \Delta t)$ tends to zero. The data in Fig. 12 clearly show the relatively insignificant effect of $(M, \Delta t)$ or R on this error in the presence of spatial discretization errors.

We find similar error behavior in comparing the $N = 1024$ case against the $N = 2048$ case, as observed in Figs. 10 and 12, except that the roughly constant error levels observed in Fig. 12 are lower by a factor of $1/4$, given the $1/2$-reduction in Δx and the second-order spatial discretization errors of the scheme. Thus, even the $N = 1024$ case is dominated by spatial discretization errors, at least up to $M = 32$, $\Delta t = 160$ ns, and $R = 10^{-5}$.

5.1.5. *Summary*

The 1D flame problem thus exhibits several of the features observed in the above simplified problem. The scheme is found to be second order in time when stiff-integration

tolerances are small. When these tolerances are large, stiff-integration errors (which are independent of Δt) are large in relation to the explicit time-integration errors, and the second-order convergence may not be observed. We also find that, for the present discretizations, the effect of splitting on the integration error is mostly exhibited through the larger global Δt, and not necessarily due to splitting per se. When the global Δt is fixed, neither M nor L has a significant effect on the error. Moreover, we have observed the role of spatial discretization errors, which evidently dominate splitting, explicit, and stiff time-integration errors for the $N = 512$ and 1024 cases.

5.2. 2D flame

Two-dimensional unsteady flame computations are very expensive, and thus do not allow the above parametric studies. We present here some results from a single computation to illustrate the performance and capabilities of the present construction. We consider the interaction of the above premixed methane–air flame with a counter-rotating 2D vortex pair. This is a typical flow that has been investigated both numerically [77, 69, 78, 79, 73, 80] and experimentally [81–86], and serves as a useful test problem.

5.2.1. *Problem Specification*

An open 2D rectangular domain is considered, with dimensions 0.4×1.6 cm^2, and is overlaid by a 256×1024 grid with uniform cell size ($\Delta x = 15.625\,\mu$m) in each coordinate direction. We apply symmetry boundary conditions in the horizontal x-direction, and outflow boundary conditions in the y-direction. The initial vorticity and temperature fields at $t = 0$ are shown in the leftmost frame of Fig. 13. The vertical right edge of the domain is the centerline of the vortex pair under consideration, which is one member of an infinite periodic row of vortex pairs along the horizontal x-direction. The initial condition

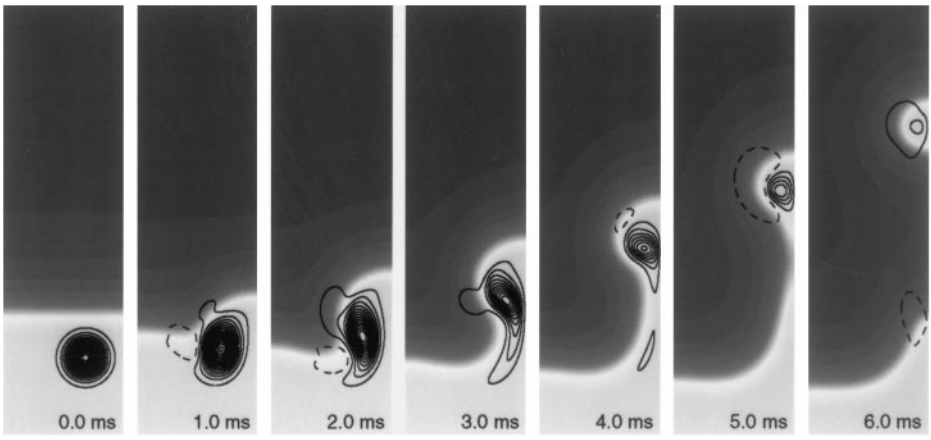

FIG. 13. Interaction of a counter-rotating vortex pair with a premixed stoichiometric 20% N_2-diluted methane–air flame using GRImech1.2 [3] over a time span of 6 ms. The shading indicates the temperature field, while solid/dashed contours delineate positive/negative vorticity. The flame propagates downward into the ambient reactants, while the vortex pair propagates upward by its self-induced velocity. Generation of a baroclinic vorticity dipole is observed due to the misalignment of the vortex-pair-induced pressure field gradient and the flame density gradient. The vortex pair contorts the flame in a manner that leads to the formation of a detached pocket of burning reactants.

is a superposition of the velocity (u, v) field induced by the periodic row of vortex pairs, and the temperature, density, and mass fraction (T, ρ, Y_i) distributions corresponding to a horizontal premixed flame, with the initial structure in the y-direction from the 1D flame shown in Fig. 5. The vorticity field corresponding to each initial vortex is a second-order Gaussian. The vortex-pair structure evolves in time, approaching a vortex doublet, with increased propagation speed. As a result, its self-induced translational velocity varies in the range 0.5–2.0 m/s. The maximum rotational velocity in the domain is around 2 m/s, giving a Mach number of 0.0067, a small value as required by the present formulation.

5.2.2. *Flow Evolution*

The results shown in Fig. 13 are computed using the operator-split stiff scheme, with $\Delta t = 200$ ns, $M = 16$, $L = 2$, $R = 10^{-6}$. The flame is observed to propagate downward, in the negative y direction, by burning into the reactants. The vorticity field causes significant contortion and large variations in the topology of the flame as the vortex pair propagates upward into it. A baroclinic vorticity dipole is generated in the neighborhood of the original vortex, in agreement with the numerical results of [77, 69, 74, 87, 4] and the experimental measurements of Mueller *et al.* [86]. The global dynamics of this flow involve penetration of the fast vortex pair into the flame, and the formation of a pocket of unburnt material carried through by the vortex pair. These dynamics reflect the relative disparity between flame and vortex-pair time scales, the ratio of which yields a Damköhler number $\mathrm{Da} = 0.4$. With $\mathrm{Da} < 1$, the flow is faster than the flame, and it is expected that some contortion of the flame will occur, as observed here.

We note that the strength of the present vortex pair and the ensuing flow time scale are 10 times smaller than those in [74] and the C_1C_2 data in [45]. As a consequence, the present flame is subjected to stretch rates that are 10 times smaller; reduced flame contortion is evident, and the rate of decay of the burning rate on the vortex-pair centerline flame segment due to the unsteady strain environment is lower. The slower flow time scale is closer to experimental conditions in [88, 85], and therefore allows improved comparisons to the corresponding measurements. The present operator-split construction is crucial for enabling the computation of this multi-millisecond flow–flame interaction given the requisite spatial resolution and stiff kinetics.

5.2.3. *Stability*

The above flow and discretization parameters lead to the following CFL numbers,

$$\lambda_c = \frac{U_{\max}\Delta t}{\Delta x} = 0.0260$$

$$\lambda_{v,M} = \frac{D_{\max}\Delta t}{\Delta x^2} = 2.49, \qquad \lambda'_{v,M} = \frac{D_{\max}\Delta t'}{\Delta x^2} = 0.156$$

$$\lambda_{v,T} = \frac{\alpha_{\max}\Delta t}{\Delta x^2} = 0.379, \qquad \lambda'_{v,T} = \frac{\alpha_{\max}\Delta t'}{\Delta x^2} = 0.0237$$

$$\lambda_{v,m} = \frac{\nu_{\max}\Delta t}{\Delta x^2} = 0.300, \qquad \lambda''_{v,m} = \frac{\nu_{\max}\Delta t''}{\Delta x^2} = 0.150,$$

where $U_{\max}$ is the maximum (u, v) velocity in the domain, and $D_{\max}$, $\alpha_{\max}$, and $\nu_{\max}$ are the largest species' diffusion coefficient, mixture thermal diffusivity, and kinematic viscosity

values, respectively. The convective CFL number λ_c is very small, well below unity. Thus, from a stability standpoint, the limiting number in this flow is clearly the viscous-CFL number in its various forms above. As indicated in Section 3.1.3, in the absence of operator splitting, experience with the non-split stiff scheme [4] suggests a diffusional stability criterion of $\lambda_v < 0.25$. Thus, in the absence of splitting, the above $\lambda_{v,M}$, $\lambda_{v,T}$, $\lambda_{v,m}$ (viscous-CFL numbers for mass, heat, and momentum) would be unstable, and the necessary maximum stable time step would be $\Delta t = 20$ ns. In the present case, $\Delta t = 200$ ns is 10 times larger, leading to significant savings, as discussed below. The above split CFL numbers ($\lambda'_{v,M}$, $\lambda'_{v,T}$, $\lambda''_{v,m}$) have been found to allow stable integration.

The critical diffusional CFL number for time integration of the above 2D flow with $M = 16$ is found empirically to be roughly 0.17, significantly smaller than 0.25. In fact, for the present M and for $L = 4$ ($\lambda'_{v,m} = 0.075$), increasing Δt to 240 ns ($\lambda'_{v,M} = 0.187$) leads to an unstable situation. Clearly, the stability limits of the operator-split scheme with $M > 0$ are different from those expected from the non-split, or split-$M = 0$, constructions. We find that the 2D critical viscous CFL number, which is 0.25 for $M = 0$, decreases monotonically with increasing M. One-dimensional tests suggest a limiting value corresponding to the AB2-diffusional stability for large M. This limit evidently becomes more significant as more AB2-diffusional sub-steps are used with increasing M.

Despite this reduction in stable viscous CFL limits due to diffusional sub-stepping, the factor of 10 increase in time step does lead to substantial computational savings. Of course, the associated speedup is expected to be less than 10-fold due to various overheads associated with the split scheme. These may be related both to the fractional time stepping for diffusion and to the stiff time-integration procedure.

5.2.4. *Stiff Integration and Operator Splitting*

Typically, we have found that (for both the split and additive constructions) the stiff ODE integration procedure in DVODE requires the most work, in terms of number of function and Jacobian evaluations ($\mathcal{F}$ and $\mathcal{J}$) as well as Newton iterations ($\mathcal{N}$), within the flame structure, where reaction rates are large. In contrast, the least work is required in the reactants. The observed maximum values of $\mathcal{F}$, $\mathcal{J}$, and $\mathcal{N}$ in the computational domain are listed in Table VIII for a range of values of $(M, \Delta t)$, for the 2D flame with $R = 10^{-6}$. These data indicate that the split scheme requires more work than the non-split scheme at the same Δt. This observation is consistent with earlier studies [48, 50, 40], where splitting the diffusion and reaction operators was found to lead to large transients in the stiff-integration phase of the scheme. These transients result in an increase of the startup cost of the ODE stiff integrator in each time step, because the integrator would have to use smaller time steps to resolve them accurately (given its specified error tolerances), which leads to increased numbers of time steps, iterations, and both function and Jacobian evaluations. In fact, we do observe that the minimum internal time step used by DVODE ($\Delta t_{\min}$) drops significantly in the split versus the non-split scheme for constant $\Delta t = 20$ ns, as seen in the table.

Moreover, there is a clear trend of increased work with increasing $(M, \Delta t)$. In fact, increasing Δt while maintaining M constant also leads to an increased stiff-integration work requirement. This is not surprising since more integration steps and evaluations are required to cover a larger time span for given error tolerance thresholds. Interestingly, the table shows that increasing Δt for constant M also leads to increased $\Delta t_{\min}$ used by DVODE. On the other hand, increasing M at constant Δt for the split scheme does not lead to more

TABLE VIII

Variation of Peak and Average Number of Function $\mathcal{F}$, Jacobian $\mathcal{J}$, and Newton Iteration $\mathcal{N}$ calls with M and Δt for the 2D flame, Using 10 Processors

M	Δt (ns)	$\mathcal{F}_{max}$	$\mathcal{J}_{max}$	$\mathcal{N}_{max}$	$\mathcal{F}_{avg}$	$\mathcal{J}_{avg}$	$\mathcal{N}_{avg}$	Δt_{min} (ns)	Speedup
32	400	110	2	109	7.47	1.02	6.47	12.8	5.8
16	200	82	2	81	5.57	1.01	4.57	7.8	4.7
8	160	68	2	67	5.15	1.00	4.15	7.4	4.7
8	100	54	1	53	4.49	1	3.49	6.3	
8	40	27	1	26	3.66	1	2.66	4.0	
4	80	46	1	45	4.23	1	3.23	5.8	2.7
4	50	30	1	29	3.80	1	2.80	4.2	
4	40	27	1	26	3.66	1	2.66	4.0	
2	40	27	1	26	3.66	1	2.66	4.0	1.5
2	25	20	1	19	3.46	1	2.46	3.0	
2	20	18	1	17	3.39	1	2.39	2.0	
0	20	9	1	8	3.14	1	2.14	7.8	1.0

Note. Also shown are the minimum internal time step (Δt_{min}) used by the stiff ODE integrator, and selective speedup data relevant to the non-split case. All cases are with $L = 0$, except for the $M = 16$, 32 cases where $L = 2$, 4, respectively.

work, and does not affect Δt_{min}, suggesting that the above stiff-integration startup transients are not dependent on the number of diffusion sub-steps. We also note that the increased work associated with large $(M, \Delta t)$ does not seem to be associated with any increase in problem stiffness due to splitting, as the amplitude of the largest eigenvalue of the system Jacobian is found to be unaffected by splitting or the number of diffusional sub-steps.

5.2.5. *Load Balancing*

It is important to point out, however, that the actual amount of work is not proportional to the peak $\mathcal{F}$, $\mathcal{J}$, and $\mathcal{N}$, but rather to their averages over the domain, which—to the extent that the flame occupies a fraction of the domain—clearly does increase with $(M, \Delta t)$ as well, but in a lower proportion. The corresponding variation in average $\mathcal{F}$, $\mathcal{J}$, and $\mathcal{N}$ is also shown in the table. As a consequence of this variable work load over the domain during the integration of the chemical source terms, care is necessary to maintain load balancing among the parallel processors. One option is to use an adaptive load balancing strategy. On the other hand, we have found that a fine-grained non-contiguous distribution of computational cells among the processors, which is efficiently done by the present shared-memory hardware (SGI Origin2000), is well suited for maintaining load balancing. This would be highly inefficient, however, on a distributed-memory machine, due to the resulting communication overheads, in which case one is compelled to implement adaptive load balancing.

5.2.6. *Scalability*

Another overhead associated with increasing M is the work corresponding to the explicit integration of the diffusion terms. The computational effort required for diffusion

can become of the same order as that of the stiff-integration procedure as M increases, particularly if the evaluation of transport coefficients is expensive. Even in the present work, where simple tabulated transport coefficients are used, in a 1D flame with $M = 16$, $R = 10^{-6}$, on an SGI Origin2000 machine with 10 R10K processors, the diffusion and reaction time-integration processes require roughly comparable 30 and 50% of the CPU time. Moreover, diffusion sub-stepping leads to reduced scalability on the present Non-uniform Memory Access (NUMA) shared-memory implementation as M is increased. This is due to the communication overhead associated with each of the consecutive (relatively non-compute-intensive) individual diffusional fractional steps. In general, the increased ratio of communication to computation is expected to lead to a reduction in scalability on both NUMA and distributed-memory hardware.

5.2.7. *Speedup*

The result of the above overheads is a speedup factor of 5, for a 2D GRImech1.2 flame on 10 processors, with $M = 16$, $L = 2$, $R = 10^{-6}$, and $\Delta t = 200$ ns, against a similar non-split implementation with $\Delta t = 20$ ns, as seen in Table VIII. Further speedup, of about $6\times$, is achieved with $M = 32$. However, the increasing overheads lead to diminishing return on further increases in M. The speedup factor increases by 80% upon doubling $(M, \Delta t)$ from (2, 40) to (4, 80). On the other hand, only 23% improvement is evident upon the doubling from (16, 200) to (32, 400).

6. CONCLUSIONS

This work has focused on the development and implementation of an operator-split numerical scheme for modeling flames in multi-dimensional unsteady flow with detailed stiff chemical kinetics. The scheme was tested using a 1D nonlinear model problem and both one- and two-dimensional flames with C_1C_2 kinetics. The construction was found to be computationally efficient, stable, and second-order accurate.

The numerical construction builds on our earlier work involving an additive non-split implicit–explicit scheme, where explicit diffusion and implicit reaction are integrated using the same global time step. The present formulation splits the diffusion and reaction operators in the scalar conservation equations using symmetric second-order Strang splitting. Each of the resulting diffusional half-steps is integrated using several sub-steps. Similarly, sub-stepping is used for the viscous terms in the momentum equations. The performance and accuracy of the scheme are governed by several parameters such as the global time step, spatial cell size, fractional time steps for scalar and momentum diffusion, and the stiff-integrator tolerances. We have outlined the relative roles of these parameters, and the necessary choices for achieving optimal performance. Generally, we find spatial errors to be dominant over time-integration errors for all cases considered. Time-integration errors are a combination of (1) explicit time-integration errors, (2) operator-splitting errors, and (3) stiff-integration errors. Operator-splitting errors were found to be relatively negligible, such that time accuracy is determined by a balance between the global time step and the stiff-integration tolerances. When the global time step is very small, the overall time-integration error is determined by the specified error thresholds used by the stiff integrator. As a consequence, the second-order convergence rate of the scheme is not empirically observable. As the global time step (and number of diffusional sub-steps) is increased, explicit

time-integration errors dominate over stiff-integration errors, which are controlled according to user-specified tolerances. When this occurs, the expected second-order convergence rate of the scheme becomes evident.

We note that the observed dominance of spatial errors, even when the flame is well resolved, suggests that there is little reason to consider higher-order ($>\Delta t^2$) time-integration constructions in the present context. In general, the utility of higher-order time-integration schemes has to be evaluated based on a study of all errors inherent in the numerical construction, and should not be a goal in and of itself. A related issue, which may be particularly delicate in conjunction with split schemes, is that of boundary conditions. In the present work, we have performed simulations in open domains only, and the tests have shown that the split schemes are globally second order. In more complex situations discretization of boundary conditions should be carefully assessed, especially when these conditions are time-dependent.

Two-dimensional reacting flow results were also presented, illustrating the interaction of a premixed methane–air flame with a counter-rotating vortex pair. A speedup factor of 5 was demonstrated, relative to the non-split stiff scheme. This speedup allows the modeling of relatively long flow–flame interaction times, in the range of 10–20 ms, on existing hardware. We are thus able to study a wider range of flow time scales, and to compare with existing experimental results utilizing relatively slow vortices. Similarly, more detailed chemical mechanisms can be utilized, affording studies of heavier hydrocarbons and their role in unsteady flame behavior.

The present experiences suggest that the performance of the scheme can be further enhanced in various ways. It may well be more efficient to use RK2 instead of AB2 in the diffusional sub-steps, thereby increasing the critical viscous-CFL number when diffusional sub-stepping is implemented. Similarly, other schemes with larger stability bounds can be considered (see, e.g., [36, 89]). Moreover, the present construction uses the same number of sub-steps for all species equations. This is in fact not necessary, as the most restrictive diffusion stability constraint is due to the high diffusivity of H, while other species and temperatures have a much lower diffusivity. A more optimal construction would use the minimum number of sub-steps necessary for the stable integration of each species, thereby reducing the diffusion time-integration effort. Given that the integration of diffusion terms is in fact a significant fraction of total CPU time, this would lead to an appreciable overall speedup of the scheme. Other approaches for improved efficiency are also under consideration, such as the utilization of adaptive mesh refinement and the enhancement of the stiff-integration efficiency by using an ODE integrator with reduced restart costs and approximate Jacobians.

APPENDIX: STIFF SPLIT CORRECTOR

In a stiff-corrector formulation of the split scheme, steps **S7** and **S8** are substituted by the following. As indicated earlier, this is not necessary, but is included here for completeness.

$\mathbf{S}_\mathrm{A}$. The diffusion term is integrated in M' fractional steps of size $\Delta t'$. The procedure is essentially identical to **S2**, except that the corrected convection source terms, C_i^* and C_ρ^*, are used in lieu of C_i^e and C_ρ^e. Thus, the AB2 fractional steps are expressed as

$$\frac{(\rho Y_i)^{k+1} - (\rho Y_i)^k}{\Delta t'} = \frac{3}{2} D_i^k - \frac{1}{2} D_i^{k-1} + \frac{1}{2} C_i^* \tag{62}$$

$$\frac{\rho^{k+1}-\rho^k}{\Delta t'} = \frac{3}{2}\left(D_\rho^k - C_{W,D}^k\right) - \frac{1}{2}\left(D_\rho^{k-1} - C_{W,D}^{k-1}\right) + \frac{1}{2}S_\rho^* \tag{63}$$

$$T^{k+1} = \frac{P_0 \bar{W}^{k+1}}{\rho^{k+1}}. \tag{64}$$

$\mathbf{S}_\mathrm{B}$. The reaction source terms are integrated over a full time step Δt, using as starting values the computed scalar fields from $\mathbf{S}_\mathrm{A}$. We also account for half the corrected convection source terms and symbolically express the integration as

$$(\rho Y_i)^{l+1} - (\rho Y_i)^l = S\int_{\Delta t}\left[\mathrm{Da}\, w_i(\rho, T, \mathbf{Y}) + \frac{1}{2}C_i^*\right]dt \tag{65}$$

$$\rho^{l+1} - \rho^l = S\int_{\Delta t}\left[-\frac{1}{c_p T}\mathrm{Da}\, w_T - C_{W,R} + \frac{1}{2}S_\rho^*\right]dt \tag{66}$$

$$T^{l+1} = \frac{P_0 \bar{W}^{l+1}}{\rho^{l+1}}. \tag{67}$$

$\mathbf{S}_\mathrm{C}$. The diffusion term is integrated in M' fractional steps of size $\Delta t'$. The procedure is identical to $\mathbf{S}_\mathrm{A}$, and the starting values are the scalar fields computed at the end of the previous step. $\mathbf{S}_\mathrm{C}$ results in the fully updated scalar fields (ρ^{n+1}, $\mathbf{Y}^{n+1}$, T^{n+1}).

ACKNOWLEDGMENTS

This work was supported by the U.S. Department of Energy (DOE), the DOE Office of Basic Energy Sciences (BES), Chemical Sciences Division, and the DOE Defense Programs Accelerated Strategic Computing Initiative (ASCI). O.M.K. acknowledges DOE/BES support as a visiting researcher at the Combustion Research Facility at Sandia National Laboratories, Livermore, California. Computations were performed at Sandia National Laboratories and at the National Center for Supercomputer Applications.

REFERENCES

1. R. Aiken (Ed.), *Stiff Computation* (Oxford Univ. Press, London, 1985).
2. E. Hairer and G. Wanner, *Solving Ordinary Differential Equations, Vol.* II, *Stiff and Differential-Algebraic Problems* (Springer-Verlag, Berlin, 1996).
3. M. Frenklach, H. Wang, M. Goldenberg, G. P. Smith, D. M. Golden, C. T. Bowman, R. K. Hanson, W. C. Gardiner, and V. Lissianski, *GRImech—An Optimized Detailed Chemical Reaction Mechanism for Methane Combustion*, Top. Rep. GRI-95/0058, GRI, 1995.
4. H. N. Najm, P. S. Wyckoff, and O. M. Knio, A semi-implicit numerical scheme for reacting flow. I Stiff chemistry, *J. Comput. Phys*. **143**(2), 381 (1998).
5. M. D. Smooke, I. K. Puri, and K. Seshadri, A comparison between numerical calculations and experimental measurements of the structure of a counterflow diffusion flame burning diluted methane in diluted air, in *Proceedings, Twenty-First Symposium (International) on Combustion* (Combustion Institute, Pittsburgh, PA, 1986), pp. 1783–1792.
6. C. F. Curtiss and J. O. Hirschfelder, Integration of stiff equations, *Proc. Nat. Acad. Sci. U.S.A.* **38**, 235 (1952).
7. C. W. Gear, *Numerical Initial Value Problems in Ordinary Differential Equations* (Prentice–Hall, Englewood Cliffs, NJ, 1971).
8. A. C. Hindmarsh, *GEAR: Ordinary Differential Equation System Solver*, Technical Report UCID-30001, Rev. 3, Lawrence Livermore National Laboratory, Livermore, CA, 1974.
9. A. C. Hindmarsh, *GEARB: Solution of Ordinary Differential Equations Having Banded Jacobian*, Technical Report UCID-30059, Rev. 2, Lawrence Livermore National Laboratory, Livermore, CA, 1977.

10. A. C. Hindmarsh, LSODE and LSODI: Two new initial value ordinary equation solvers, *ACM-SIGNUM* **15**(4), 10 (1980).
11. A. C. Hindmarsh, ODEPACK: A systematized collection of ODE solvers, in *Scientific Computing*, edited by R. Stepleman (North-Holland, Amsterdam, 1983), pp. 55–64.
12. P. N. Brown, G. D. Byrne, and A. C. Hindmarsh, VODE: A variable coefficient ODE solver, *SIAM J. Sci. Statist. Comput*. **10**, 1038 (1989).
13. P. J. Vanderhouven and B. P. Sommeijer, Analysis of parallel diagonally implicit iteration of Runge–Kutta methods, *Appl. Numer. Math*. **11**, 169 (1993).
14. N. H. Cong, A parallel DIRK method for stiff initial-value problems, *J. Comput. Appl. Math*. **54**, 121 (1994).
15. X. Zhong, Additive semi-implicit Runge–Kutta methods for computing high-speed nonequilibrium reactive flows, *J. Comput. Phys*. **128**, 19 (1996).
16. J. J. B. Baeza, F. P. Plá, and G. R. Ramos, Stiffness–adaptive Taylor method for the integration of non-stiff and stiff kinetic models, *J. Comput. Chem*. **13**, 810 (1992).
17. P. Sun, D. P. Chock, and S. L. Winkler, An implicit–explicit hybrid solver for a system of stiff kinetic equations, *J. Comput. Phys*. **115**, 515 (1994).
18. D. P. Chock, S. L. Winkler, and P. Sun, Comparison of stiff chemistry solvers for air quality modeling, *Environ. Sci. Technol*. **28**, 1882 (1994).
19. D. Dabdub and J. H. Seinfeld, Extrapolation techniques used in the solution of stiff ODEs associated with chemical kinetics of air quality models, *Atmos. Environ*. **29**, 403 (1995).
20. S. Elliot, R. P. Turco, and M. Z. Jacobson, Tests on combined projection/forward differencing integration for stiff photochemical family systems at long time step, *Computers Chem*. **17**, 91 (1993).
21. E. Hesstvedt, O. Hov, and I. S. A. Isaksen, Quasi-steady-state approximations in air pollution modeling: Comparison of two numerical schemes for oxidant prediction, *Int. J. Chem. Kinetics* **10**, 971 (1978).
22. T. R. Young and J. P. Boris, A numerical technique for solving stiff ordinary differential equations associated with the chemical kinetics of reactive flow problems, *J. Phys. Chem*. **81**, 2424 (1977).
23. J. G. Verwer and M. van Loon, An evaluation of explicit pseudo-steady-state approximation schemes for stiff ODE systems from chemical kinetics, *J. Comput. Phys*. **113**, 347 (1994).
24. W. Gong and H.-R. Cho, A numerical scheme for the integration of the gas-phase chemical rate equations in three-dimensional atmospheric models, *Atmos. Environ*. **27A**, 2591 (1993).
25. R. D. Saylor and G. D. Ford, On the comparison of numerical methods for the integration of kinetic equations in atmospheric chemistry and transport models, *Atmos. Environ*. **29**(19), 2585 (1995).
26. H. H. Robertson, The solution of a set of reaction rate equations, in *Numerical Analysis: an Introduction*, edited by J. Walsh (Academic Press, New York, 1966), pp. 178–182.
27. K. Radhakrishnan, New integration techniques for chemical kinetic rate equations. I. Efficiency comparison, *Combust. Sci. Technol*. **46**, 59 (1986).
28. Y. D'Angelo and B. Larrouturou, Comparison and analysis of some numerical schemes for stiff complex chemistry problems, *RAIRO Modél. Math. Anal. Numér*. **29**, 259 (1995).
29. J. G. Verwer, Gauss–Seidel iteration for stiff ODES from chemical kinetics, *SIAM J. Sci. Comput*. **15**, 1234 (1994).
30. J. G. Verwer, J. G. Blom, and E. J. Spee, A comparison of stiff ODE solvers for atmospheric chemistry problems, *Atmos. Environ*. **30**, 49 (1996).
31. C. J. Aro, CHEMSODE: A stiff ODE solver for the equations of chemical kinetics, *Comput. Phys. Commun*. **97**, 304 (1996).
32. R. Courant, K. O. Friedrichs, and H. Lewy, Über die Partiellen Differenzengleichungen der Mathematischen Physik, *Math. Ann*. **100**, 32 (1928); Translation, On the partial difference equations of mathematical physics, *IBM J. Res. Develop*. **11**, 215 (1967).
33. D. A. Anderson, J. C. Tannehill, and R. H. Pletcher, *Computational Fluid Mechanics and Heat Transfer* (Hemisphere, New York, 1984).
34. C. A. J. Fletcher, *Computational Techniques for Fluid Dynamics* (Springer-Verlag, Berlin, 1988), Vol. I.
35. J. M. Varah, Stability restrictions on second order, three level finite difference schemes for parabolic equations, *SIAM J. Numer. Anal*. **17**(2), 300 (1980).

36. U. M. Ascher, S. J. Ruuth, and B. T. R. Wetton, Implicit–explicit methods for time-dependent partial differential equations, *SIAM J. Numer. Anal*. **32**(3), 797 (1995).
37. W. Hundsdorfer and J. G. Verwer, A note on splitting errors for advection–reaction equations, *Appl. Numer. Math.* **18**, 191 (1995).
38. J. G. Verwer, J. G. Blom, and W. Hundsdorfer. An implicit–explicit approach for atmospheric transport-chemistry problems, *Appl. Numer. Math*. **20**, 191 (1996).
39. P. Sun, A pseudo-non-time-splitting method in air quality modeling, *J. Comput. Phys.* **127**, 152 (1996).
40. J. G. Verwer, E. J. Spee, J. G. Blom, and W. H. Hundsdorfer, A second order Rosenbrock method applied to photochemical dispersion problems, *SIAM J. Sci. Comput.* **20**, 1456 (1999).
41. J. Frank, W. Hundsdorfer, and J. G. Verwer, On the stability of implicit–explicit linear multistep methods, *Appl. Numer. Math*. **25**, 193 (1997).
42. O. Knoth and R. Wolke, Implicit–explicit Runge–Kutta methods for computing atmospheric reactive flows, *Appl. Numer. Math*. **28**, 327 (1998).
43. J. G. Verwer, and D. Simpson, Explicit methods for stiff ODEs from atmospheric chemistry, *Appl. Numer. Math*. **18**, 413 (1995).
44. O. Knoth and R. Wolke, An explicit–implicit numerical approach for atmospheric chemistry-transport modeling, *Atmos. Environ*. **32**, 1785 (1998).
45. H. N. Najm, O. M. Knio, P. H. Paul, and P. S. Wyckoff, A study of flame observables in premixed methane–air flames, *Combust. Sci. Technol*. **140**(1–6), 369 (1998).
46. W. H. Hundsdorfer, *Numerical Solution of Advection–Diffusion–Reaction Equations*, Lecture Notes, Report NM-N9603, CWI, Amsterdam, 1996; http://info4u.cwi.nl.
47. E. J. Spee, Coupling advection and chemical kinetics in a global atmospheric test model, in *Air Pollution III*, edited by H. Power *et al.* (Computational Mechanics, Southampton-Boston, 1995), Vol. 1, pp. 319–326.
48. J. G. Verwer, J. G. Blom, M. van Loon, and E. J. Spee, A comparison of stiff ODE solvers for atmospheric chemistry problems, *Atmos. Environ*. **30**, 49 (1995).
49. E. J. Spee, P. M. de Zeeuw, J. G. Verwer, J. G. Blom, and W. H. Hundsdorfer, *Vectorization and Parallelization of a Numerical Scheme for 3D Global Atmospheric Transport-Chemistry Problems*, Report NM-R9620, CWI, Amsterdam, 1996; http://info4u.cwi.nl.
50. E. J. Spee, J. G. Verwer, P. M. de Zeeuw, J. G. Blom, and W. Hundsdorfer, A numerical study for global atmospheric transport-chemistry problems, *Math. Comput. Simulation* **48**, 177 (1998).
51. L. A. Khan and P. L.-F. Liu, An operator splitting algorithm for coupled one-dimensional advection–diffusion–reaction equations, *Comput. Methods Appl. Mech. Eng*. **127**, 181 (1995).
52. Q. Sheng, Solving linear partial differential equations by exponential splitting, *IMA J. Numer. Anal*. **9**, 199 (1989).
53. J. P. Wright, Numerical instability due to varying time steps in explicit wave propagation and mechanics calculations, *J. Comput. Phys*. **140**, 421 (1998).
54. R. J. LeVeque and H. C. Yee, A study of numerical methods for hyperbolic conservation laws with stiff source terms, *J. Comput. Phys*. **86**, 187 (1990).
55. D. Lanser and J. G. Verwer, Analysis of operator splitting for advection–diffusion–reaction problems from air pollution modelling, CWI Report NM-R9805; http://info4u.cwi.nl.
56. G. Strang, On the construction and comparison of difference schemes, *SIAM J. Numer. Anal*. **5**(3), 506 (1968).
57. S. Z. Burstein and A. A. Mirin, Third order difference methods for hyperbolic equations, *J. Comput. Phys*. **5**, 547 (1970).
58. H. Yoshida, Construction of higher order symplectic integrators, *Phys. Lett. A* **150**(5–7), 262 (1990).
59. G. Goyal, P. J. Paul, H. S. Mukunda, and S. M. Deshpande, Time dependent operator-split and unsplit schemes for one dimensional premixed flames, *Combust. Sci. Techol*. **60**, 167 (1988).
60. B. Yang and S. B. Pope, An investigation of the accuracy of manifold methods and splitting schemes in the computational implementation of combustion chemistry, *Combust. Flame* **112**, 16 (1998).
61. A. Majda and J. Sethian, The derivation and numerical solution of the equations for zero Mach number combustion, *Combust. Sci. Technol*. **42**, 185 (1985).

62. H. Schlichting, *Boundary-Layer Theory* (McGraw–Hill, New York, 1979), 7th ed.
63. F. A. Williams, *Combustion Theory* (Addison–Wesley, New York, 1985), 2nd ed.
64. R. J. Kee, F. M. Rupley, and J. A. Miller, *Chemkin-II: A Fortran Chemical Kinetics Package for the Analysis of Gas Phase Chemical Kinetics*, Sandia Report SAND89-8009B, Sandia National Laboratories, Livermore, CA, 1993.
65. A. J. Chorin, A numerical method for solving incompressible viscous flow problems, *J. Comput. Phys*. **2**, 12 (1967).
66. J. B. Bell and D. L. Marcus, A second-order projection method for variable density flows, *J. Comput. Phys*. **101**, 334 (1992).
67. A. S. Almgren, J. B. Bell, and M. L. Welcome, A conservative adaptive projection method for the variable density incompressible Navier–Stokes equations, *J. Comput. Phys*. **142**, 1 (1998).
68. P. A. McMurtry, W.-H. Jou, J. J. Riley, and R. W. Metcalfe, Direct numerical simulations of a reacting mixing layer with chemical heat release, *AIAA J*. **24**(6), 962 (1986).
69. C. Rutland, J. H. Ferziger, and B. J. Cantwell, *Effects of Strain, Vorticity, and Turbulence on Premixed Flames*, Report TF-44, Thermosciences Division, Mechanical Engineering, Stanford University, Stanford, CA, 1989.
70. C. J. Rutland and J. H. Ferziger, Simulations of flame–vortex interactions, *Combust. Flame* **84**, 343 (1991).
71. S. Mahalingam, B. J. Cantwell, and J. H. Ferziger, Full numerical simulations of coflowing, axisymmetric jet diffusion flames, *Phys. Fluids A* **2**, 720 (1990).
72. J. Kim and P. Moin, Application of a fractional-step method to incompressible Navier–Stokes equations, *J. Comput. Phys*. **59**, 308 (1985).
73. H. N. Najm, A conservative low Mach number projection method for reacting flow modeling, in *Transport Phenomena in Combustion*, edited by S. Chan (Taylor & Francis, Washington DC, 1996), Vol. 2, pp. 921–932.
74. H. N. Najm and P. S. Wyckoff, Premixed flame response to unsteady strain-rate and curvature, *Combust. Flame* **110**(1–2), 92 (1997).
75. H. N. Najm, O. M. Knio, and P. S. Wyckoff, Response of stoichiometric and rich methane–air flames to unsteady strain-rate and curvature, submitted for publication.
76. R. J. Kee, J. F. Grcar, M. D. Smooke, and J. A. Miller, *A Fortran Program for Modeling Steady Laminar One-Dimensional Premixed Flames*, Sandia Report SAND85-8240, Sandia National Laboratories, Livemore, CA, 1993.
77. W. T. Ashurst and P. A. McMurtry, Flame generation of vorticity: Vortex dipoles from monopoles, *Combust. Sci. Technol*. **66**, 17 (1989).
78. T. Poinsot, D. Veynante, and S. Candel, Quenching processes and premixed turbulent combustion diagrams, *J. Fluid Mech*. **228**, 561 (1991).
79. T. Mantel, *Fundamental Mechanisms in Premixed Flame Propagation via Vortex–Flame Interactions—Numerical Simulations*, Annual research briefs, Center for Turbulence Research, Stanford University/NASA Ames Research Center, 1994.
80. M. Hilka, D. Veynante, M. Baum, and T. J. Poinsot, Simulation of flame–vortex interactions using detailed and reduced chemical kinetics, in *Proceedings, Tenth Symposium on Turbulent Shear Flows, Penn. State University, University Park, PA, 1995*, Vol. 2, Section 19, pp. 19–24.
81. J. Jarosinski, J. H. Lee, and R. Knystautas, Interaction of a vortex ring and a laminar flame, in *Proceedings, Twenty-Second Symposium (International) on Combustion* (Combustion Institute, 1988), pp. 505–514.
82. W. L. Roberts, J. F. Driscoll, M. C. Drake, and L. P. Goss, Images of the quenching of a flame by a vortex—To quantify regimes of turbulent combustion, *Combust. Flame* **94**, 58 (1993).
83. J.-M. Samaniego, *Stretch-Induced Quenching in Flame-Vortex Interactions*, Annual research briefs, Center for Turbulence Research, Stanford University/NASA Ames Research Center, 1993.
84. C. J. Mueller, J. F. Driscoll, D. J. Sutkus, W. L. Roberts, M. C. Drake, and M. D. Smooke, Effect of unsteady stretch rate on OH chemistry during a flame–vortex interaction: To assess flamelet models, *Combust. Flame* **100**, 323 (1995).
85. Q.-V. Nguyen and P. H. Paul, The time evolution of a vortex–flame interaction observed via planar imaging of CH and OH, in *Proceedings, Twenty-Sixth Symposium (International) on Combustion* (Combustion Institute, 1996), pp. 357–364.

86. C. J. Mueller, J. F. Driscoll, D. L. Reuss, M. C. Drake, and M. E. Rosalik, Vorticity generation and attenuation as vortices convect through a premixed flame, *Combust. Flame* **112**(3), 342 (1998).
87. H. N. Najm, P. H. Paul, C. J. Mueller, and P. S. Wyckoff, On the adequacy of certain experimental observables as measurements of flame burning rate, *Combust. Flame* **113**(3), 312 (1998).
88. P. H. Paul and H. N. Najm, Planar laser-induced fluorescence imaging of flame heat release rate, in *proceedings, 27th Symposium (International) on Combustion* (Combustion Institute, 1998), pp. 43–50.
89. J. G. Verwer, Explicit Runge–Kutta methodsfor parabolic partial differential equations, *Appl. Numer. Math*. **22**, 359 (1996).